SAND2015-7476R

International Collaborations on Fluid Flows in Fractured Crystalline Rocks: FY15 Progress Report

Fuel Cycle Research & Development

Prepared for
U.S. Department of Energy
Used Fuel Disposition

Yifeng Wang, Payton Gardner,
Kristopher L. Kuhlman
Sandia National Laboratories
Mohammad Lutful Kabir, Sung-Hoon Ji
Korean Atomic Energy Research Institute

August 25, 2015

FCRD-UFD-2015-000711

Sandia National Laboratories is a multi-program laboratory managed and operated by Sandia Corporation, a wholly owned subsidiary of Lockheed Martin Corporation, for the U.S. Department of Energy's National Nuclear Security Administration under contract DE-AC04-94AL85000.

FCT Quality Assurance Program Document

Appendix E
FCT Document Cover Sheet

Name/Title of Deliverable/Milestone	International collaborations on fluid flows in fractured crystalline rocks: FY15 progress report (M4FT-15SN0807082)
Work Package Title and Number	Crystalline Disposal R&D (International)
Work Package WBS Number	FT-15SN080708
Responsible Work Package Manager	Yifeng Wang (Name/Signature)

Date Submitted 8/13/2015

Quality Rigor Level for Deliverable/Milestone	☐ QRL-3	☐ QRL-2	☐ QRL-1 ☐ Nuclear Data	☒ N/A*

This deliverable was prepared in accordance with Sandia National Laboratories
(Participant/National Laboratory Name)

QA program which meets the requirements of
☒ DOE Order 414.1 ☐ NQA-1-2000

This Deliverable was subjected to:

☐ Technical Review

Technical Review (TR)
Review Documentation Provided
☐ Signed TR Report or,
☐ Signed TR Concurrence Sheet or,
☐ Signature of TR Reviewer(s) below

Name and Signature of Reviewers
N/A

☐ Peer Review

Peer Review (PR)
Review Documentation Provided
☐ Signed PR Report or,
☐ Signed PR Concurrence Sheet or,
☐ Signature of PR Reviewer(s) below

*Note: In some cases there may be a milestone where an item is being fabricated, maintenance is being performed on a facility, or a document is being issued through a formal document control process where it specifically calls out a formal review of the document. In these cases, documentation (e.g., inspection report, maintenance request, work planning package documentation or the documented review of the issued document through the document control process) of the completion of the activity along with the Document Cover Sheet is sufficient to demonstrate achieving the milestone. QRL for such milestones may be also be marked N/A in the work package provided the work package clearly specifies the requirement to use the Document Cover Sheet and provide supporting documentation.

INTERNATIONAL COLLABORATIONS ON FLUID FLOWS IN FRACTURED CRYSTALLINE ROCKS: FY15 PROGRESS REPORT

EXECUTIVE SUMMARY

Active participation in international R&D is crucial for achieving the UFD long-term goals of conducting "experiments to fill data needs and confirm advanced modeling approaches" (by 2015) and of having a "robust modeling and experimental basis for evaluation of multiple disposal system options" (by 2020). DOE's Office of Nuclear Energy (NE) and its Office of Used Fuel Disposition Research and Development (UFD) have developed a strategic plan to advance cooperation with international partners. The international collaboration on the evaluation of crystalline disposal media at Sandia National Laboratories (SNL) in FY15 was focused on the following three activities: (1) thermal-hydrologic-mechanical-chemical modeling single fracture evolution; (2) simulations of flow and transport in Bedrichov Tunnel, Czech Republic, and (3) streaming potential testing at Korean Atomic Energy Research Institute (KAERI) Underground Research Tunnel (KURT). The first two activities are part of the Development of Coupled Models and their Validation against Experiments (DECOVALEX) project. The major accomplishments include:

- *DECOVALEX C.1: Thermal-Hydrologic-Mechanical-Chemical (THMC) Processes in Single Fractures:* A mechanistic understanding of fracture opening and closure in geologic media is of significant importance to subsurface resource extraction and waste isolation (e.g. radioactive waste disposal and carbon sequestration and storage). It has been observed that, under certain circumstances, a fracture can undergo either opening or closure or switch from one regime to another. Fracture evolution involves a complex set of coupled physical and chemical processes, including stress-mediated mineral dissolution and precipitation, fluid flow and transport, mechanical deformation, etc. A dynamic model for subsurface fracture opening and closure was formulated. The model explicitly accounts for the stress concentration around individual aperture channels and the stress-activated mineral dissolution and precipitation. A preliminary model analysis has demonstrated the importance of the stress-activated dissolution mechanism in the evolution of fracture aperture in a stressed geologic medium. The model provides a reasonable explanation for some key features of fracture opening and closure observed in laboratory experiments, including a spontaneous switch from a net permeability reduction to a net permeability increase with no changes in experimental conditions.
- *DECOVALEX C.2: Bedrichov Tunnel Test Case:* A lumped parameter model was developed for stable isotope, tritium and CFC-12 transport at the site and modeled results were compared to measured data. Code PFLOTRAN was used to simulate multiple environmental tracer concentrations in heterogeneous 2D and 3D domains. The comparison of the models between different teams shows that for the most part the teams are able to match the results among each other. Understanding the discrepancies between models has proved to be a great learning experience for all teams and improved the understanding of the underlying mechanics of each code, and each codes strengths and limitations. The models reported here have been developed to understand the residence time distribution and transport properties of fractured crystalline rocks. The models are capable of reproducing the gross characteristics of hydraulic and tracer

transport. The reasons for discrepancy between models and observation and methods to improve the fit are actively being explored. The DECOVALEX 2015 modeling is producing new insight into modeling transport in fracture systems over long scales and time periods of years. These types of data sets are valuable for both developing modeling techniques and understanding of long-term transport processes in fractured rock. Natural tracer data sets are of time scales much closer to repository performance prediction than most applied tracer experiments. The utilization of long-term data sets such as those provided by natural tracers allows us to gain more confidence in the prediction of long term transport.

- *KAERI Underground Research Tunnel Tests:* SNL and KAERI have developed a multi-year plan for joint field testing and modeling to support the study of high-level nuclear waste disposal in crystalline geologic media. The work for FY15 is focused on two tasks: (1) streaming potential (SP) testing, and (2) technique development for in-situ borehole characterization. A sandbox experiment was established at KAERI to study the hydroelectric coupling in case of a tracer test. An acrylic tank was filled up with homogeneous sand as a sand aquifer, and the upstream and downstream reservoirs were connected to the sand aquifer to control the hydraulic gradient. Under a steady-state water flow condition, a tracer test was performed in the sandbox with the help of peristaltic pump, and tracer samples were collected from the same interval of five screened wells in the sandbox. During the tracer test, SP signals resulting from the distribution of 20 nonpolarizable electrodes were measured at the top of the tank by a multichannel meter. The results showed that there were changes in the observed SP after injection of tracer, which indicated that the SP was likely to be related to the solute transport. For Task 2, SNL have finalized a new contract with KAERI on a collaborative work the development of in-situ hydrological and geochemical measurements in boreholes. This task is a jointed effort between the UFD deep borehole disposal work package and the crystalline disposal R&D work package.
- *Joint Fuel Cycle Studies (JFCS):* A technical exchange meeting was held under the JFCS bilateral between the Republic of Korea (ROK) and the US DOE. Extensive technical data exchanges between the two parties have proceeded.

Future work will include: (1) developing a plan for the participation in the new phase of the DECOVALEX project; (2) continuing to work closely with KAERI on the streaming potential testing at the KURT site; (3) initiating an actual field test at the KURT site for the development of in-situ measurement techniques in boreholes; and (4) identifying new opportunities for the newly excavated tunnel at the KURT site.

CONTENTS

1. OBJECTIVES

Recognizing the benefits of international collaboration in the common goal of safely and efficiently managing the back end of the nuclear fuel cycle, DOE's Office of Nuclear Energy (NE) and its Office of Used Fuel Disposition Research and Development (UFD) have developed a strategic plan to advance cooperation with international partners (Birkholzer et al., 2013; UFD, 2012). UFD's strategic plan lays out two interdependent areas of international collaboration. The first area is cooperation with the international nuclear community through participation in international organizations, working groups, committees, and expert panels. Such participation typically involves conference and workshop visits, information exchanges, reviews, and training and education. The second area of international collaboration is active R&D participation of U.S. researchers within international projects or programs (UFD, 2012). By active R&D, it is meant that U.S. researchers work closely together with international scientists on specific R&D projects relevant to both sides. With respect to geologic disposal of radioactive waste, such active collaboration provides direct access to information, data, and expertise on various disposal options and geologic environments that have been collected internationally over the past decades. Many international programs have operating underground research laboratories (URLs) in clay/shale, granite, and salt environments, in which relevant field experiments have been and are being conducted. Depending on the type of collaboration, U.S. researchers can participate in planning, conducting, and interpreting experiments in these URLs, and thereby get early access to field studies without having in situ research facilities in the United States.

UFD considers this second area, active international R&D, to be very beneficial in achieving the program's long-term goals of conducting "experiments to fill data needs and confirm advanced modeling approaches" (by 2015) and of having a "robust modeling and experimental basis for evaluation of multiple disposal system options" (by 2020). Advancing opportunities for active international collaboration with respect to geologic disposal has therefore been the primary focus of UFD's international strategy in the recent year (Birkholzer et al., 2013; Birkholzer, 2012).

This report summarizes the work accomplished in FY15 at Sandia National Laboratories (SNL) related to international collaborations on the evaluation of crystalline rocks as disposal media. The FY15 work was focused on the the following three activities: (1) thermal-hydrologic-mechanical-chemical modeling single fracture evolution; (2) simulations of flow and transport in Bedrichov Tunnel, Czech Republic, and (3) streaming potential testing at Korean Atomic Energy Research Institute (KAERI) Underground Research Tunnel (KURT). The first two activities are part of the Development of Coupled Models and their Validation against Experiments (DECOVALEX) project. This work directly supports the following UFD objectives:

- Develop a fundamental understanding of disposal system performance in a range of environments for potential wastes that could arise from future nuclear fuel cycle alternatives through theory, simulation, testing, and experimentation.
- Develop a computational modeling capability for the performance of storage and disposal options for a range of fuel cycle alternatives, evolving from generic models to more robust models of performance assessment.

The work documented here also addresses the following specific topics identified based on the UFD R&D Implementation Plan (Wang, 2014).

- Topic #S5: Evaluation of state of the art of site characterization techniques
- Topic #S7: Identification of the needs for using underground research laboratory
- Topic #P1: Development of discrete fracture network model
- Topic #P2: Parameter estimation and uncertainty quantification of field testing

1.1 REFERENCES

Birkholzer, J.T. (2012). Status of UFD Campaign International Activities in Disposal Research. Report prepared for U.S. Department of Energy Used Fuel Disposition Campaign, FCRD-UFD-2012-000295.

Birkholzer, J., Asahina, D., Chen, F., Gardner, P., Houseworth, J., Jove-Colon, C., Kersting, A., Nair, P., Nutt, M., Li, L., Liu, H.H., Painter, S., Reimus, P., Rutqvist, J., Steefel, C., Tynan, M., Wang, Y., Zavarin, M. (2013). An overview of US disposal research activities linked to international URLs. Proceedings of the 2013 International High-Level Radioactive Waste Management Conference (IHLRWM), April 28 – May 2, 2013, Albuquerque, New Mexico.

UFD (2012). Office of Used Fuel Disposition International Program — Strategic Plan (2013) April 2012, U.S. Department of Energy.

Wang, Y. (2014) Used Fuel Disposal in Crystalline Rocks: Status and FY14 Progress, FCRD-UFD-2014-000060.

2. DYNAMICS OF SUBSURFACE FRACTURE OPENING AND CLOSURE: THEORY

2.1 INTRODUCTION

A mechanistic understanding of fracture opening and closure in geologic media is of significant importance to subsurface resource extraction and waste isolation (e.g. radioactive waste disposal and carbon sequestration and storage) (e.g., Yasuhara et al., 2006; Ellis et al., 2013). It has been observed that, under certain circumstances, a fracture can undergo either opening or closure or switch from one regime to another (Polak et al., 2004; Liu et al., 2006; McGuire et al., 2013). Fracture evolution involves a complex set of coupled physical and chemical processes, including stress-mediated mineral dissolution and precipitation, fluid flow and transport, mechanical deformation, etc. Significant effort has been made to understand these processes, especially in laboratory-scale experiments. For example, in a flow-through experiment on a natural fracture in novaculite under moderate effective stress, Yasuhara et al. (2006) observed a reduction in fracture permeability for the first 1500 hours followed by a significant increase in fracture aperture as the temperature was ramped above the room temperature. In a similar experiment on a limestone fracture, Polak et al. (2004) observed that, during the initial circulation of groundwater, the differential pressure increased about threefold as the contacting asperities across the fracture were removed. Interestingly, after switching to the circulation of distilled water, they first observed a further threefold permeability reduction and then a spontaneous switch from a net permeability reduction to a net permeability increase with no changes in experimental conditions. The underlying mechanism for this switch is not well understood. Also, in a limestone fracture, an increase in fracture permeability is usually accompanied with the development of preferential dissolution channelings (Elkhoury et al., 2013). Various models have been developed for the interpretation of experimental observations (Yasuhara et al., 2004, 2006; Liu et al., 2006). Unfortunately, no existing model is able to provide a consistent explanation for key experimental observations.

The objective of this paper is to lay a theoretical foundation for modeling the dynamics of subsurface fracture opening and closure. The model proposed below explicitly accounts for stress concentration around individual fracture apertures and the resulting stress-mediated mineral dissolution and precipitation. A preliminary model analysis shows that this model is able to explain key features of fracture opening and closure observed in laboratory column experiments.

2.2 MODEL FORMULATION

Geometric representation of a single fracture

It is assumed that a fracture plan can be represented with isolated contacting asperities and connected aperture channels that run through between the asperities (Figure 2-1). It is further assumed that the cross section of an individual aperture channel can be described by a truncated ellipse defined by the intersection of two identical ellipses (Figure 2-2):

$$\frac{x'^2}{a'^2} + \frac{(y'-h)^2}{b'^2} = 1 \quad (2\text{-}1)$$

$$\frac{x'^2}{a'^2} + \frac{(y'+h)^2}{b'^2} = 1 \quad (2\text{-}2)$$

where x' and y' are the local coordinates; and a' and b' are the major and minor semi-axes of the ellipses respectively. Parameters a' and b' are related to the semi-axes of the truncated ellipse (a, b) by (Figure 2-2):

$$a' = \frac{h+b}{\sqrt{(h+b)^2-h^2}}a \quad (2\text{-}3)$$

$$b' = h + b. \quad (2\text{-}4)$$

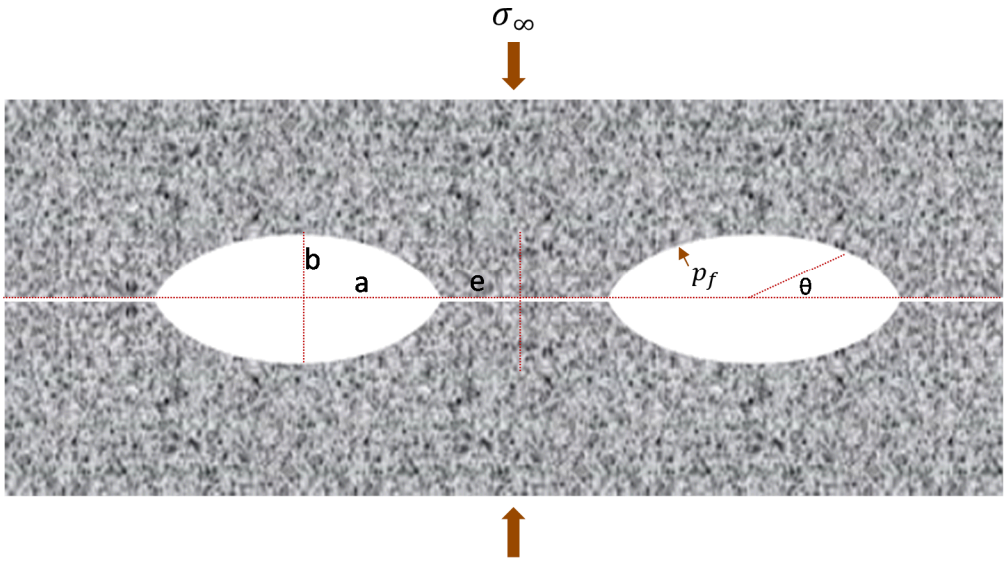

Figure 2-1: Representation of a single fracture plane with truncated elliptic channels surrounding isolated fracture contact areas.

The area of the cross section (S) can be calculated by:

$$S = 1a'b' \arcsin\left(\frac{a}{a'}\right) - 2ha \quad (2\text{-}5)$$

The contact area ratio of a fracture can be defined by:

$$f_c = 1 - \alpha\sqrt{1-\left(1-\frac{b}{b'}\right)^2} \quad (2\text{-}6)$$

with

$$\alpha = \frac{a'}{a_0 + e_0}$$

where a_0 and e_0 are the initial width of the aperture channel (a) and the contact area (b) respectively. As shown in Figure 2-3, Equation (2-6) is able to fit the measured aperture-contact area relation fairly well, implying that the geometry of an actual aperture channel can be represented adequately by a truncated ellipse. This geometrical representation has certain advantages over other geometries such as a triangular representation (Liu et al., 2006), which is not able to reproduce the measured aperture-contact area ratios.

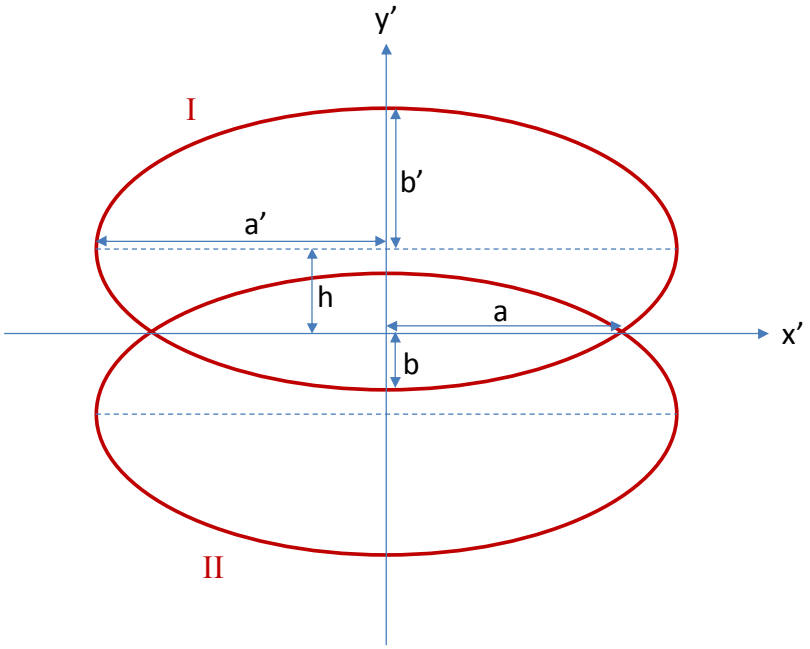

Figure 2-2: Geometric representation of a truncated elliptic channel

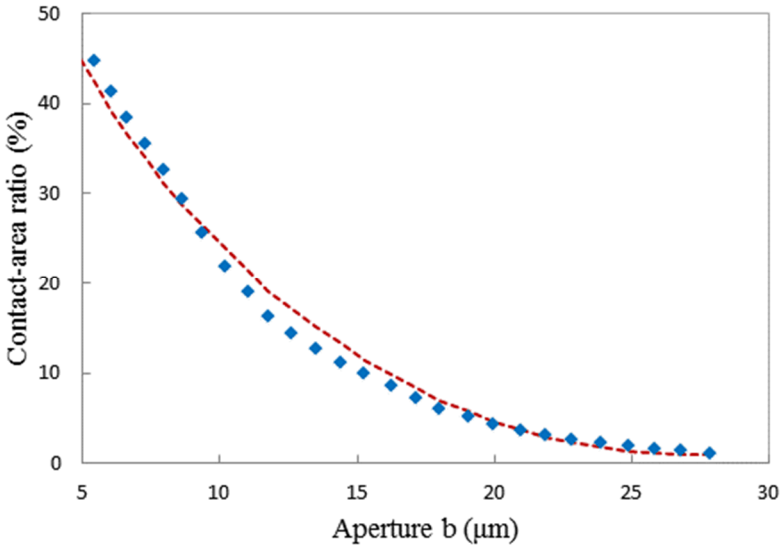

Figure 2-3: Model fitting to the measured aperture and contact-area relation. Data are taken from Yasuhara et al. (2006)

Local stress

The model proposed here explicitly accounts for the stress concentration at the fracture contact areas and on the surface of aperture channels as a result of a far-field compressive normal stress (σ_∞) applied (Figure 2-1). For simplicity, it is assumed that, for the stress calculation, the geometry of a truncated elliptic channel can be approximately represented by a normal ellipse. The stress at any point of fracture surface is broken into two orthogonal components: the normal stress and the tangential stress (Chung and Fuller, 1992). Adopting the convention of a compressive stress to be positive, we have:

At a fracture contact:

$$\sigma_\infty = p_f(1 - f_c) + \sigma_c^n f_c \quad (2\text{-}7)$$

$$\sigma_c^t = p_f \quad (2\text{-}8)$$

where p_f is the pore fluid pressure; σ_c^n and σ_c^t are the normal stress and tangential stress at the contact, respectively.

Similarly, on an aperture surface (Reuschlé et al., 1988), we have:

$$\sigma_p^n = p_f \quad (2\text{-}9)$$

$$\sigma_p^t(\theta) = p_f - \frac{(1-m^2)(-\sigma_\infty+2p_f)+2\sigma_\infty(m-cos2\theta)}{1+m^2-2mcos2\theta} \quad (2\text{-}10)$$

where $m = (a-b)/(a+b)$; σ_p^n and σ_p^t are the normal stress and tangential stress on the surface; and θ is the eccentric angle of the point under consideration on the aperture surface (Figure 2-1).

It is assumed that the shape of an aperture channel remains to be a truncated ellipse during fracture evolution. In this way, we can focus ourselves only on two specific locations on a channel surface θ = 0 or π/2:

$$\sigma_p^t(0) = p_f + \frac{(3-m)\sigma_\infty-2(1+m)p_f}{1-m} \quad (2\text{-}11)$$

$$\sigma_p^t\left(\frac{\pi}{2}\right) = p_f - \frac{(1+m)\sigma_\infty+2(1-m)p_f}{1+m}. \quad (2\text{-}12)$$

Elastic strain energy:

It is assumed that the rock involved in fracture opening and closure behaves elastically. The strain energy at each location can be calculated as (Reuschlé et al., 1988):

At a fracture contact:

$$\Delta G_s(contact) = \frac{1}{2}\left(\frac{{\sigma_c^n}^2+{\sigma_c^t}^2}{E} - \frac{2\nu}{E}\sigma_c^n \cdot \sigma_c^t\right) \quad (2\text{-}13)$$

On an aperture surface:

$$\Delta G_s(0) = \frac{v_s}{2}\left[\frac{\sigma_p^n(0)^2+\sigma_p^t(0)^2}{E} - \frac{2\nu}{E}\sigma_p^n(0) \cdot \sigma_p^t(0)\right] \quad (2\text{-}14)$$

$$\Delta G_s\left(\frac{\pi}{2}\right) = \frac{v_s}{2}\left[\frac{\sigma_p^n\left(\frac{\pi}{2}\right)^2+\sigma_p^t\left(\frac{\pi}{2}\right)^2}{E} - \frac{2\nu}{E}\sigma_p^n\left(\frac{\pi}{2}\right) \cdot \sigma_p^t\left(\frac{\pi}{2}\right)\right] \quad (2\text{-}15)$$

where $\Delta G_s(\cdot)$ is the strain energy at a specific location; v_s is the molar volume of the mineral involved; E is the Young's modulus; and ν is the Poisson's ratio.

The contribution of elastic strain energy to the total Gibbs free energy of a mineral is generally small and has been ignored in many geochemical calculations (Bruton and Helgeson, 1983). However, this treatment is not adequate in the case considered here, because the major driving force for mineral dissolution and precipitation within aperture channels and at fracture contacts is the chemical potential difference between the nearby mineral surfaces instead of the total Gibbs free energy of the mineral.

Chemical potential and stress-activated mineral dissolution

The chemical potential at a specific point of a fracture surface depends on the local stress at that location. It can be expressed as a function of both normal and tangential stresses on the surface. At a fracture contact, we have:

$$\mu_s = \mu_s^0 + \sigma_c^n v_s + \Delta G_s(contact) \tag{2-16}$$

$$\mu_a = \mu_a^0 + \sigma_c^n v_a + RTlnC_c \tag{2-17}$$

where μ_s and μ_a are the chemical potentials of the mineral of concern and the corresponding dissolved species respectively; μ_s^0 and μ_a^0 are the chemical potentials at the standard state at a given temperature and pressure; v_a is the molar volume of the dissolved species; C_c is the concentration of the dissolved species at the fracture contact; R is the gas constant; and T is the absolute temperature. The second terms on the right-hand side of Equations (2-16) and (2-17) represent the work done by the normal stress as a reacting surface retreats or advances (Guéguen and Palciauskas, 1994). It is assumed that a thin water film exists at a fracture contact and this film is able to sustain the normal stress across the contact.

The chemical affinity (A_c) for mineral dissolution at a fracture contact is calculated by:

$$A_c = \mu_s - \mu_a = \mu_s^0 - \mu_a^0 + \sigma_c^n(v_s - v_a) + \Delta G_s(contact) - RTlnC_c \tag{2-18}$$

Based on the transition state theory, the dissolution rate of a fracture surface can be described by (de Groot and Mazur, 1984; Dove, 1995):

$$R(contact) = kTe^{-\frac{\Delta G^{\ddagger} + \sigma_c^t v^{\ddagger}}{RT}}\left(1 - e^{-\frac{A_c}{RT}}\right)$$

$$= kTe^{-\frac{\Delta G^{\ddagger} + p_f v^{\ddagger}}{RT}}\left[1 - \frac{C_c}{K(contact)}\right] \tag{2-19}$$

where k is the reaction rate constant; $\Delta G^{\ddagger}$ is the activation energy to account for the temperature effect on the reaction rate; $v^{\ddagger}$ is the activation volume to account for the effect of surface stress on the reaction rate (Aziz et al., 1991; Yu and Suo, 2000); and $K(contact)$ is the equilibrium constant of the dissolution reaction under stress:

$$K(contact) = e^{\frac{\mu_s^0 - \mu_a^0 + \sigma_c^n(v_s - v_a) + \Delta G_s(contact)}{RT}}. \tag{2-20}$$

Similarly, the dissolution rate at an aperture surface can be expressed by:

$$R(0) = kTe^{-\frac{\Delta G^{\ddagger} + \sigma_p^t(0) v^{\ddagger}}{RT}}\left[1 - \frac{C_p}{K(0)}\right] \tag{2-21}$$

$$R\left(\frac{\pi}{2}\right) = kTe^{-\frac{\Delta G^{\#} + \sigma_p^t\left(\frac{\pi}{2}\right)v^{\#}}{RT}}\left[1 - \frac{C_p}{K\left(\frac{\pi}{2}\right)}\right] \quad (2\text{-}22)$$

where C_p is the concentration of dissolved species in the aperture. The equilibrium constant on the aperture surface can be expressed by:

$$K(0) = e^{\frac{\mu_s^0 - \mu_a^0 + p_f(v_s - v_a) + \Delta G_S(0)}{RT}} \quad (2\text{-}23)$$

$$K\left(\frac{\pi}{2}\right) = e^{\frac{\mu_s^0 - \mu_a^0 + p_f(v_s - v_a) + \Delta G_S\left(\frac{\pi}{2}\right)}{RT}}. \quad (2\text{-}24)$$

Note that the concept of stress-activated mineral dissolution is an important component of the proposed model. This concept is based on the experimental observations that a tensile tangential stress at a solid surface enhances both mineral dissolution and growth at the surface (Aziz et al., 1991; Barvosa-Carter and Aziz, 1998; Yu and Suo, 2000). The activation volume $v^{\#}$ is estimated to be ~ 0.28 v_s (Aziz et al., 1991).

Reaction-diffusion at a contact

The mass transfer between a fracture contact and the surrounding aperture channels proceeds through a diffusion process driven by a chemical potential difference ($\Delta\mu$):

$$\Delta\mu = \left(\sigma_c^n - p_f\right)v_a + RTln\frac{C_c}{C_p} \quad (2\text{-}25)$$

For a unit length of an aperture channel, the mass exchange between the aperture and the contact can be described by:

$$Dw\frac{\Delta\mu}{e} = 2eR(contact)$$

$$Dw\left[\left(\sigma_c^n - p_f\right)v_a + RTln\frac{C_c}{C_p}\right] = 2e^2R(contact) \quad (2\text{-}26)$$

where w is the thickness of the water film at the contact and D is the diffusion coefficient of the dissolved species. The thickness of the water film depends on the confining stress across the fracture plan, the surface properties of minerals (e.g., surface charge density) and the chemistry of channel fluid. For simplicity, the following functional relationship is adopted to capture the effect of the confining stress on water film thickness (Renard and Ortoleva, 1997):

$$w = \beta(\sigma_c^n - p_f)^\gamma \quad (2\text{-}27)$$

where β and γ (< 0) are adjustable constants. The water film becomes thinner as the confining stress σ_c^n increases.

Kinematics of pore evolution

In the proposed model, the geometry of fracture aperture and contact is determined by four independent variables: *a*, *b*, *h*, and *e* (Figures 2-1 and 2-2). The evolution of fracture geometry is described by the following kinematic equations:

$$\frac{da}{dt} = v_s R(0) - \frac{da}{db} v_s R(contact) = -v_s R(0) - \frac{ha'^2}{ab'^2} v_s R(contact) \quad (2\text{-}28)$$

$$\frac{db}{dt} = -v_s R(contact) + v_s R\left(\frac{\pi}{2}\right) \quad (2\text{-}29)$$

$$\frac{dh}{dt} = -v_s R(contact) \quad (2\text{-}30)$$

$$l_0 = a + e = a_0 + e_0 \quad (2\text{-}31)$$

The last term in Equation (2-28) captures the effect of fracture asperity dissolution on the contact-area ratio of the fracture.

From local to global

Up to this point, the model is presented only in a local coordinate (*x'*, *y'*) (Figure 2-2). To model fracture evolution on a whole fracture plane, this local description needs to be incorporated into global-scale mass continuity equations. In a global coordinate (*x*, *y*), variables *a*, *b*, *h*, and *e* not only evolve with time but also vary in space. The pore volume per unit fracture area can be defined as:

$$\phi = \frac{b(1-f_c)S}{4ab} \quad (2\text{-}32)$$

The tortuosity of aperture channels (τ) is assumed to be:

$$\tau = \frac{1}{1-f_c} \quad (2\text{-}33)$$

in analog to that defined for porous media (Oelkers, 1996). The permeability at each spatial point on a fracture plane can be calculated by (Lekner, 2007):

$$K = \frac{\pi(1-f_c)S(ab)^3}{16\eta b l_0(a^2+b^2)} \quad (2\text{-}34)$$

assuming that the flow field in a truncated elliptic channel can be approximated by a normal elliptic channel with the same semi-axes. Similarly, the diffusion efficient of the dissolved species can be calculated by:

$$D = \frac{(1-f_c)S}{4ab} D_0 \quad (2\text{-}35)$$

D_0 is the diffusion coefficient in water. The mass continuity equations for the fluid and the dissolved species in the global coordinate can then be expressed by:

$$\frac{\partial \phi}{\partial t} = \vec{\nabla} \cdot (K \vec{\nabla} p_f) \tag{2-36}$$

$$\frac{\partial (\phi C_p)}{\partial t} = \vec{\nabla} \cdot \left(D \vec{\nabla} C_p + K C_p \vec{\nabla} p_f \right) + \frac{1}{2 l_0 v_s} \frac{\partial S}{\partial t} + 2R(contact) \tag{2-37}$$

2.3 PRELIMINARY MODEL ANALYSIS

The model proposed above has been tested against experimental observations on circular channels (Sprunt and Nur, 1977). In those experiments, a rectangular slab of a selected material with a centrically drilled hole was used (i.e., the cross section of the initial hole is circular). The slab was loaded uniaxially, producing non-uniform circumferential stress along the surface of the hole. The surface was kept in contact with a chemically reactive solution. The experiments showed that the dissolution on a free surface was to a large extent controlled by the tangential stress (i.e. the stress parallel to the surface), but not by the normal stress. Various shapes were induced by stress-mediated surface dissolution, notably ellipses perpendicular to the uniaxial stress applied and ellipses parallel to the stress (Table 1). Interestingly, the ellipses perpendicular to the stress tended to occur in the material with the solutions saturated with the material, while the ellipses parallel seemed to occur in undersaturated solutions. Increasing the applied uniaxial stress could lead to the switch from a perpendicular ellipse to a parallel ellipse.

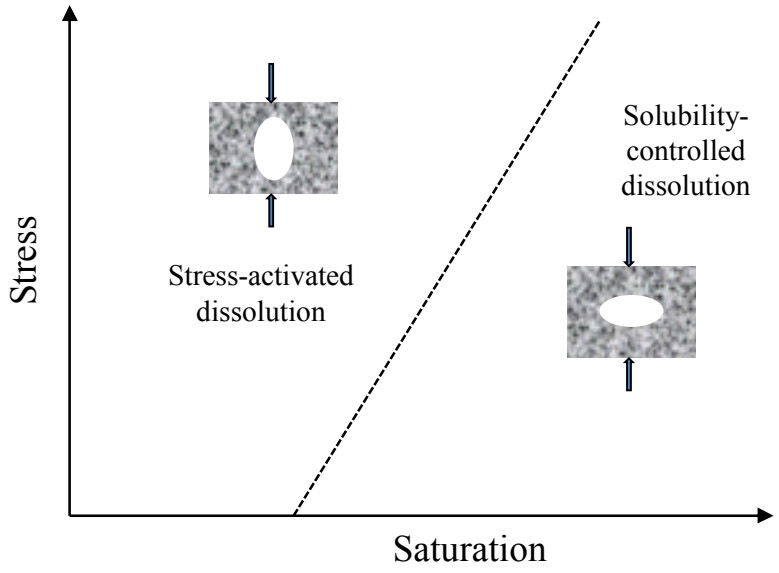

Figure 2-4: Schematic illustration of the evolution of an initially circular hole under stress

Based on the model presented above, the shape evolution of an initially circular channel is determined by the ratio of $R\left(\frac{\pi}{2}\right)$ to $R(0)$:

$$g = e^{\frac{4\sigma_\infty v^\#}{RT}} \frac{1-\widetilde{C_p}e^{-\frac{v_S\sigma_\infty^2}{2ERT}}}{1-\widetilde{C_p}e^{-\frac{9v_S\sigma_\infty^2}{2ERT}}} \quad (2\text{-}38)$$

where $\widetilde{C_p}$ is the saturation degree of the channel fluid with respect to the mineral of concern under no stress conditions:

$$\widetilde{C_p} = C_p / e^{\frac{\mu_S^0-\mu_a^0}{RT}}$$

The derivation of Equation (38) is based on the following considerations:

- For a circular channel, *m = 0* in Equations (2-11) and (2-12). Thus, $\sigma_p^t(0) = 3\sigma_\infty$ and $\sigma_p^t\left(\frac{\pi}{2}\right) = -\sigma_\infty$.
- $\sigma_p^n = p_f \ll \sigma_p^t(0)$ or $\sigma_p^t\left(\frac{\pi}{2}\right)$. Thus, σ_p^n can be negligible in Equations (2-14) and (2-15).

In a situation with $g > 1$, the dissolution would lead to the development of an ellipse parallel to the uniaxial stress applied, whereas, in a case with $g < 1$, the dissolution would lead to an ellipse perpendicular to the stress. The g value depends on two factors. When the channel fluid is very undersaturated, the g value depends only on the stress activation term $e^{\frac{4\sigma_\infty v^\#}{RT}}$ in Equation (38), and is always greater than unity. In this case, an ellipse parallel to the uniaxial stress would develop (Figure 2-4). In contrast, as the saturation degree increases, the term $(1-\widetilde{C_p}e^{-\frac{v_S\sigma_\infty^2}{2ERT}})/(1-\widetilde{C_p}e^{-\frac{9v_S\sigma_\infty^2}{2ERT}})$ in the Equation would take over the stress activation term, resulting in $g < 1$ and therefore an ellipse perpendicular to the uniaxial stress (Figure 2-4). The model prediction agrees well with experimental observations (Table 2-1). The model analysis has thus demonstrated the importance of the stress-activation mechanism in the evolution of fracture aperture in a stressed geologic medium. This mechanism has not been considered in any other existing models.

Table 2-1: Resulting shape of an initially circular hole due to stress-mediated dissolution (Sprunt and Nur, 1977)

Material & solution	Axial load (bars)	Hole shape
Solenhofen limestone 3	129	Ellipse parallel
Solenhofen limestone 4	66	Ellipse parallel
Solenhofen limestone 6	45	Ellipse perpendicular
Salt undersaturated 1	30	Ellipse parallel
Salt undersaturated 2	12	Ellipse parallel
Salt undersaturated 3	13	Ellipse parallel
Salt saturated 1	15	Ellipse perpendicular
Salt saturated 2	14	Ellipse perpendicular

In the model presented above, the aperture of a fracture can be represented by the minor semi-axis of the truncated ellipse ($2b$). From Equation (2-29), the criteria for fracture opening or closure can be formulated as:

$$-v_s R(contact) + v_s R\left(\frac{\pi}{2}\right)\begin{cases} > 0 & \text{fracture opening} \\ < 0 & \text{fracture closure} \end{cases} \tag{2-39}$$

A qualitative model analysis indicates that the following conditions would favor fracture opening: a high fluid flow rate, a low saturation degree of the channel fluid, a high confining stress, and a high contact area ratio. In an actual subsurface system, the last two conditions can be easily satisfied; however, the first two seem hard to maintain. Assume that the incoming water is initially undersaturated with the minerals involved. But this water would rapidly become saturated as it percolates through the fracture, eventually leading to fracture closure. In this sense, in a natural subsurface environment, fractures tend to close. The situation could be different for an engineered subsurface system, for example, for acid injection for enhanced oil recovery, in which the injected fluid can be maintained highly reactive by continuous fluid circulation. The model formulated above may help design an effective strategy for fracture opening for a specific engineering application.

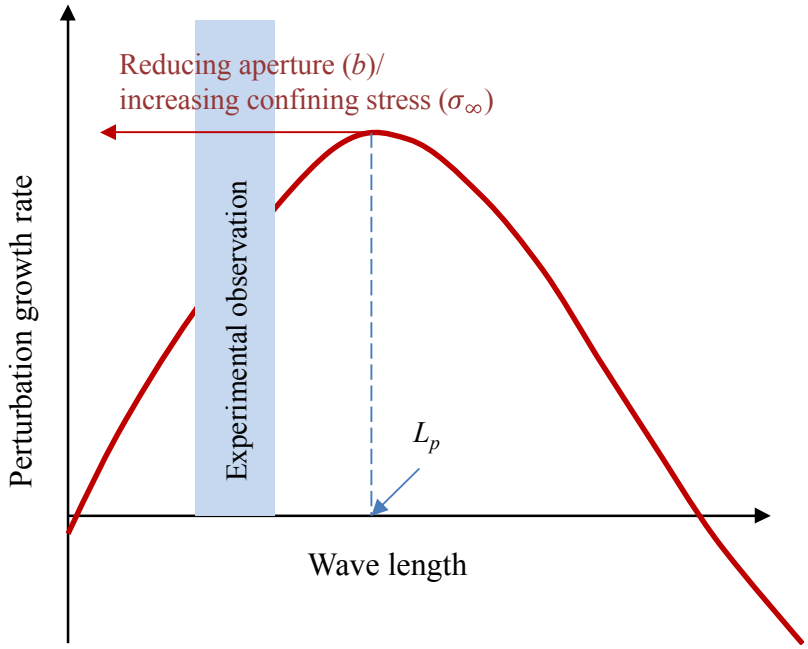

Figure 2-5: Spontaneous initiation of aperture channeling. As the fracture aperture reduces due to pressure dissolution, the preferred wave length of dissolution fingering decreases. Once the preferred wave length falls within the experimental observation range, a spontaneous initiation of preferential channeling can be observed.

One way for fracture opening is preferential channeling (Elkhoury et al., 2013). Fracture channeling is induced by fluid infiltration instability (Szymczak and Ladd, 2012). Because of this instability, certain modes of fluctuations (or perturbations) in fracture aperture can be amplified, leading to the fingering of a dissolution front. The actual spacing of the resulting fingers (L_c) is determined by the maximum growth rate of the perturbations (Figure 2-5). Combined the model formulation presented above with a linear stability analysis performed by Szymczak and Ladd (2012), we obtain:

$$L_p \propto \frac{b^3}{kT} e^{\frac{\Delta G^{\ddagger} - \sigma_\infty \left(\frac{\pi}{2}\right) v^{\ddagger}}{RT}} \tag{2-40}$$

Equation (2-40) shows that, as the fracture aperture (b) reduces due to pressure dissolution, the spacing of the fingers decreases. Once the wave length of fingering falls within the experimental observation range, a spontaneous initiation of preferential channeling can then be observed (Figure 2-5). This may be responsible for the observed spontaneous switch from a net permeability reduction to a net permeability increase with no changes in a limestone fracture experiment (Polak et al., 2004).

2.4 CONCLUSIONS

A dynamic model for subsurface fracture opening and closure has been formulated. The model explicitly accounts for the stress concentration around individual aperture channels and the stress-activated mineral dissolution and precipitation. A preliminary model analysis has demonstrated the importance of the stress-activated dissolution mechanism in the evolution of fracture aperture in a stressed geologic medium. The model provides a reasonable explanation for some key features of fracture opening and closure observed in laboratory experiments, including a spontaneous switch from a net permeability reduction to a net permeability increase with no changes in a limestone fracture experiment.

2.5 REFERENCES

Aziz, M. J., Sabin, P. C. and Lu. G.-Q. (1991) The activation strain tensor: Nonhydrostatic stress effects on crystal-growth kinetics, Phys. Rev. B, 44, 9812-9816.

Barvosa-Carter, W. Aziz, M. J. (1998) Kinetically driven growth instability in stressed solids, Phys. Rev. Letters, 81, 1445-1448.

Bruton, C. J. and Helgeson, H. C. (1983) Calculation of the chemical and thermodynamic consequences of differences between fluid and geostatic pressure in hydrothermal systems, Am. J. Sci., 283-A, 540-588.

Chuang, T.-J. and Fuller, Jr., E. (1992) Extended Charles-Hillig Theory for stress corrosion cracking of glass, 75, 540-545.

De Groot, S. R. and Mazur P. (1984) Non-Equilibrium Thermodynamics, North-Holland Pub. Co., Amsterdam.

Dove, P. M. (1995) Geochemical controls on the kinetics of quartz fracture at subcritical tensile stresses, J. Geophys. Res., 100, 22349-22359.

Elkhoury, J. E., Ameli, P. and Detwiler, R. L. (2013) Dissolution and deformation in fractured carbonates caused by flow of CO2-rich brine under reservoir conditions, Inter. J. Greenhouse Gas Control, 16S, S203-S212.

Ellis, B. R., Fitts, J. P., Bromhal, G. S., McIntyre, D. L., Rappero, R. and Peters, C. A. (2013) Dissolution-driven permeability reduction of fractured carbonate caprock, Envriron. Eng. Sci., 30, 187-193.

Guéguen, Y. and Palciauskas, V. (1994) Introduction to the Physics of Rocks, Princeton University Press, Princeton, N.J.

Lekner, J. (2007) Viscous flow through pipes of various cross-sections, Eur. J. Phys., 28, 521-527.

Liu, J., Sheng, J., Polak, A., Elsworth, D., Yasuhara, H. and Grader, A. (2006) A fully-coupled hydrological-mechanical-chemical model for fracture sealing and preferential opening, Inter. J. Rock Mech. Ming Sci., 43, 23-36.

McGuire, T. P., Elsworth, D., and Karcz, Z. (2013) Experimental measurements of stress and chemical controls on the evolution of fracture permeability, Transp. Porous Med., 98, 15-34.

Oelkers, E. H. (1996) Phyical and chemical properties of rocks and fluids for chemical mass transport calculations, Review in Mineralogy, 34, 131-191.

Polak, A., Elsworth, D., Liu, J. and Grader, A. S. (2004) Spontaneous switching of permeability changes in a limestone fracture with net dissolution, Water Resources Res., 40, W03502.

Renard, F. and Ortoleva, P. (1997) Water films at grain-grain contacts: Debye-Hückel, osmotic model of stress, salinity, and mineralogy dependence, Geochim. Cosmochim. Acta, 61, 1963-1970.

Reuschlé, T., Trotignon, L. and Gueguen, Y. (1988) Pore shape evolution by solution transfer: thermodynamics and mechanics, Geophys. J., 95, 535-547.

Sprunt, E. S. and Nur, A. (1977) Experimental study of the effects of stress on solution rate, J. Geophys. Res., 82, 3013-3022.

Szymczak, P. and Ladd, A. J. C. (2012) Reactive-infiltration instabilities in rocks. Fracture dissolution, J. Fuid Mech., 702, 239-264.

Yasuhara, H. and Elsworth, D. (2004) Evolution permeability in a natural fracture: Significant role of pressure solution, J. Geophys. Res., 109, B03204.

Yasuhara, H., Polak, A., Mitani, Y., Grader, A. S., Halleck, P. M., and Elsworth, D. (2006) Evolution of fracture permeability through fluid-rock reaction under hydrothermal conditions, Erath Planet Sci. Letters, 244, 186-200.

Yu, H. H. and Suo, Z. (2000) Stress-dependent surface reactions and implications for a stress measurement technique, 87, 1211-1218.

3. DECOVALEX 2015 - TASK C2: MODELING OF FLOW AND TRANSPORT AT BEDRICHOV SITE

3.1 INTRODUCTION

DECOVALEX 2015 Task C2 is designed to investigate fractured rock transport processes in the Bedrichov Tunnel of the Czech Republic. The Bedrichov tunnel task is based mainly on the measured tunnel inflow flowrate and isotopic composition. The main issue is inhomogeneity of water flow, i.e. distribution of water to conduits of different size/scale (faults, fractures), relation of water quantity and flow velocity (or residence time). The other is uncertainty evaluation from calibration and blind prediction steps with partial data available and from cross-validating with different models (e.g. hydraulics and tracers). The data provided for this task are mostly obtained by Technical University of Liberec (TUL) but some of them are from other organizations participating on the research. Within the Decovalex-2011, the Test Case was solved with the data from the site, mostly as a hydraulic problem, in 3D with full digital terrain model.

The Task is based on data from Bedrichov tunnel (

Figure 3-1), located in Jizera mountains, north of the Czech Republic, part of the Bohemian massif, Krkonoše-Jizera Composite Massif. The tunnel was excavated during 1980-1981, first 890m from SW with TBM method and remaining part by drill-and-blast. The last part of approx. 150m on the reservoir bottom is constructed from the surface. The research related to the Bedrichov site in the context of nuclear waste repository host rock started in 2003, with support of RAWRA, led by J. Klomínský from Czech Geological Survey, with participation of several other institutes. The site is important as one of the few underground spaces in the hard host rock available for research in the Czech Republic. The site is a water supply tunnel in operation, which is also used for research, by agreement with the operator, SCVK Ltd. The research has been supported by RAWRA from 2003 as industrial analogue of the repository conditions. Within the Decovalex-2011, the Test Case was solved with the data from the site. The site is important as one of the few underground spaces in the hard host rock available for research in the Czech Republic, considering the purpose-built underground laboratory is not planned.

The basic study is hydraulics, followed by conservative transport and reactive transport. In the hydraulic model, the modelling issue and challenge is mostly in transition from discrete fractures to equivalent continuum (finding reasonable scale of inhomogeneity in the model according to available data) related to distribution of water inflow. The conservative transport model, linked to the natural tracer data, solves in the first level, the standard problem of fitting the single inflow data with lumped parameter models. In the second level, 2D or 3D advection model is planned, to connect the various inflow points in a single model and to cross-validate the transport model with the hydraulic model. The third part, reactive transport models, has similar sequence, from fitting the laboratory (batch) experiments of granite leaching with e.g. general geochemical models, to reactive transport (possibly 1D) model with site-specific geometric and hydraulic data fitted to composition of particular inflow water in the tunnel. One aim in the numerical modeling context is to fit the water inflow and the natural tracer concentration with lumped parameter models and 3D hydraulic-transport models.

This section is adopted from a draft report for DECOVALEX Task C2, contributed by Milan Hokr and Aleš Balvín (TUL, Czech), Hua Shao and Herbert Kunz, (Bundesanstalt für Geowissenschaften und Rohstoffe, Germany) and William Payton Gardner and Yifeng Wang (SNL, USA).

3.2 PROBLEM SPECIFICATION

Site features

The tunnel length is 2600 m, straight in the full length in the azimuth 67° (the orientation to coordinates is discussed below). The first 890 m from SW is excavated with TBM method and remaining part by drill-and-blast. The diameter of the TBM part is 3.6 m, the size of the D&B part is similar but irregular. There are irregularly distributed intervals of bare rock and shotcrete (both in TBM and D&B) but the shotcrete is rather exceptional in the TBM part. In the shallowest parts (first 110 m and last approx.300 m) stronger stabilization is installed.

The altitude of the lower (SWW) end is 657 m and the upper (NEE) end is 697 m. The slope is thus approx. 1.5 %. The highest hill above the tunnel is 820 m altitude, the reservoir dam is 735 m and water level typically 732 m altitude. The last approx. 100-150 m of the tunnel is directly under the reservoir water level.

Most inflow is concentrated in the shallow parts, in the interval 50 m-100 m inflow is collected in installed hoses, while in the interval 2200 m-2450 m inflow includes smaller leakage points in the shotcrete and several larger inflow locations collected in tubing. In the deeper part there are fully dry intervals, short intervals with some leakage (but not freely flowing water) and several places (faults/fractures) with medium strong inflow. The more precise quantification is presented below. For the measurements, a set of single inflow springs was selected, representing the range of inflow types: deep/shallow, strong/wear, bare-rock fracture/shotcreted fault structure.

Measured data

The following measurements are available (and selected will provided to keep the task partly as blind prediction):

- “manual” measurement of inflow in 7 points (springs) unevenly distributed in the tunnel but representing different types of flow and rock, measured from 2006 in 14 days intervals, data from one or two years will be provided
- “manual” measurement of collecting channel flowrate in the tunnel portal (from 2006 in 14 days intervals), this is quite little precise
- “manual” measurement of collecting canal flowrate in four places in the tunnel twice in 2004, separating inflow from five tunnel sections
- Automatic (continual) measurement of inflow in the above 7 points installed sequentially from 2010 to now /it is still to be determined which parts to provide for calibration/
- Single measurement of collecting canal flowrate with dilution method in 2012, better separating totalized inflow from more tunnel sections
- Automatic canal flowrate measurement on four weirs installed recently (no real data yet)

Input or boundary conditions measurements include:

- temperature and precipitation data collected from meteorological stations nearby operated by other institutions (different resolution from day to hour depending on year), from 2010 collected systematically
- own meteorological station with soil temperature and humidity from Apr 2011 (15 min intervals)
- water infiltration recorded by lysimeter (determined amount) from Jan 2010 and soil water content probes (only events qualitatively) from Nov 2011, but some problems in operation and not sure to be fully representative for recharge to deeper rock
- reservoir water level, flow rate in selected streams nearby (hourly), and chemical composition of precipitation (monthly) collected from other institutions
- soil temperature is measured in two places (forest, meadow) above the tunnel from Aug 2008 with some outages

Model definition

We consider a model without exact terrain shape, representing a part of the tunnel in the particular depth, with scheme given in

Figure 3-2. Use of symmetric quarter for numerical solution is recommended. An effect of mixing water from slow flow through the massif and quicker flow through a fracture/fault is included schematically. Also, division of shallow more permeable and deep less permeable part is necessary and described below.

The particular solution can include any of the equivalent continuum, discrete fracture network, and hybrid models (with different way of representation of the more and less conductive domains), but the concept is aimed for combination of 3D domain of rock continuum and 2D domain of fault/fracture.

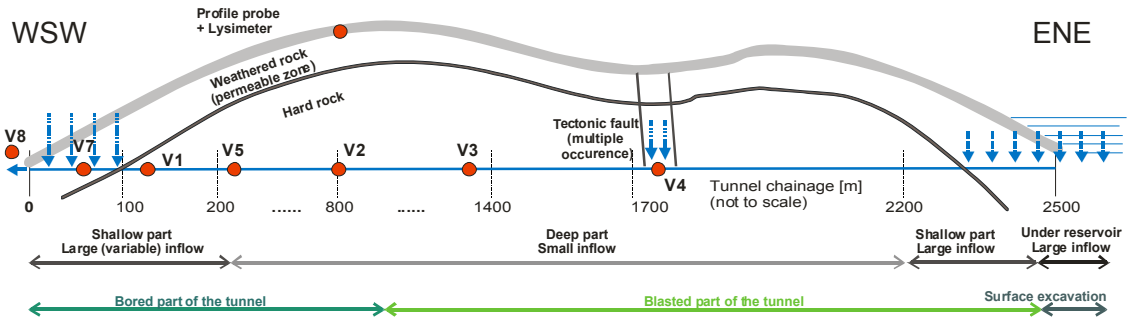

Figure 3-1: Tunnel profile – technical and hydrogeological conditions

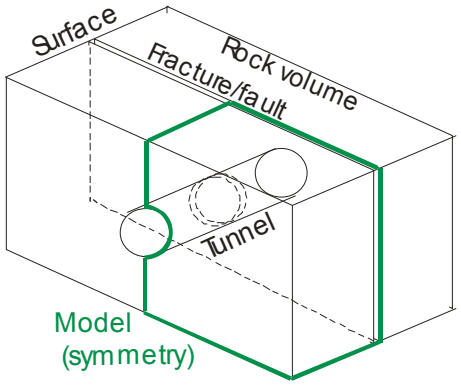

Figure 3-2: Model concept for particular place in the tunnel distinguishing the inflow from a fracture/fault and rock continuum (matrix or network of smaller fractures)

1.1.1 Model geometry and configuration: We consider a model without exact terrain shape, representing a part of the tunnel in the particular depth, with scheme given in

1.1.2

1.1.3

1.1.4

Figure 3. Use of symmetric quarter for numerical solution is recommended. An effect of mixing water from slow flow through the massif and quicker flow through a fracture/fault is included schematically. Also, division of shallow more permeable and deep less permeable part is necessary and described below.

The dimensions are 600 m width perpendicular to the tunnel (300 m for symmetric model), 400 m depth and 200 m width along the tunnel (100 m for symmetric model – on each side of the fracture. Variable depth of permeable zone is considered, defined in Table 3-1.

The particular solution can include any of the equivalent continuum, discrete fracture network, and hybrid models (with different way of representation of the more and less conductive domains), but the concept is aimed for combination of 3D domain of rock continuum and 2D domain of fault/fracture.

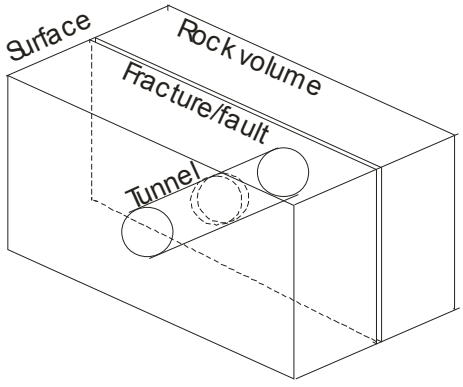

Figure 3-3: Model scheme for representing non-uniform water inflow to a tunnel

Four particular configurations for this concept are used to represent selected typical tunnel segments around measured inflow (

Figure , Table 3-1), in the respective order:

- Model 1: interval 0-100 m (shallow weathered layer), measured inflow position 70 m (V7), aggregated all inflow in the real segment is considered for the model
- Model 2: interval 100-250 m (hard rock just below the shallow weathered zone), measured inflow positions 125 m (V1 – drops from a single fracture), 142 m (larger inflow from a fracture set), 225 m (single fracture with continuous flow)
- Model 3: position 798 m (deep in compact rock, weak inflow) – measured V2 (drops)
- Model 4: position 1728 m (deep, fault zone 5-20 m width) – measured V4

We define three basic components of the model: 3D shallow zone with the hydraulic conductivity K_1, 3D deep zone with the hydraulic conductivity K_2 and vertical fracture or fault with the transmissivity T_f (possibly evaluated from given thickness and hydraulic conductivity). In each scheme, the left part is a vertical section along the tunnel (grey strip) and the right part is a vertical section perpendicular to the tunnel (grey circle).

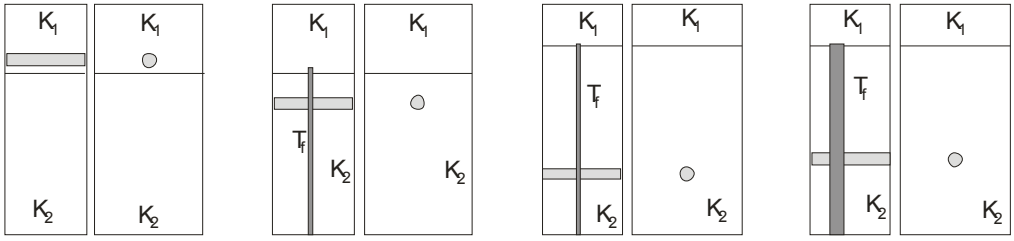

Figure 3-4: Particular model configuration (1-4) representing selected real positions in the tunnel (for the numerical discretisation, it is convenient to consider the fracture/fault domain up to the surface).

Table 3-1: Parameters for the four model configurations

	Model 1	Model 2	Model 3	Model 4
notation	spring V7, 70m	spring V1,V5,V6 (3 sub-variants)	spring V2	spring V4
position along the tunnel	70m	120-250m	798m	1728m
characteristics	shallow strong	shallow weak	deep week	deep strong
	weathered layer	single fracture	single fracture	fault zone
dimensions/positions				
depth [m]	-23	-39 (common/ individual)	-140	-91
boundary weathered/compact [m]	-26	-25	-15	-20
hydraulic conditions				
gw table max [m] (wet period)	0	0	0	0
gw table min [m] (dry period)	"-21 (or -26)	-21	-15	0
typical inflow				
inflow distributed - density m3/s/m	zero or 7.8e-6 to 3.1e-5 (time dependent) **1.5e-5 average**	5.00E-08	**5.00E-10**	5.00E-08
inflow fracture - flux mililiter/s	none	V1: 2e-2 to 5e-2	2.00E-02	20
		V5: 3.0	less time dep	negligible time dependent
		V6: 8.0 to 14.0 (time dependent)		

Inclined model: We consider a new model, M1, with inclined terrain shape, representing a large-scale model and partly including terrain surface (Figure 3-4 right). The M1 inclined model concept is aimed for including the hydraulic effect of variable precipitation on the water table in a hill slope in the entrance part of the tunnel (Figure 3-5 right). The dimensions are 400 m width perpendicular to the tunnel (reduced to 200 m in a symmetric half model used for numerical calculation), 400-580 m height and 1000 m width along the tunnel. Use of symmetric half for numerical solution is considered by the vertical plane along the tunnel axis.

We assume that width of model is enough because of the tunnel drains only part of the hill slope. The hill slope is derived from the real terrain shape above the tunnel – the elevation difference of 170 meters along the 1000 m distance. The position of the tunnel is 10 m above the valley bottom. The geometry is relevant to the reality in sense that the length of the tunnel section in the permeable shallow zone is approximately 100 m.

As the boundary conditions, we prescribe infiltration on the slope (average estimated value is 200 mm per year, later considered variable) and the zero (atmospheric) pressure on the tunnel walls. On the vertical side below the valley, in its upper part corresponding to the permeable zone, we prescribe piezometric head to simulate underground creek runoff – the main domain discharge before the tunnel inflow. On the other sides, we prescribe no flow boundary condition (Figure 3-5b).

The measurements of the tunnel inflow in this part fluctuates approximately between 300 ml/a (during period without precipitation) and 1.5 l/s in the peaks of wet events with heavy infiltration. There are two kinds of data for the inflow, one is the seepage site V7 which is relatively accurately measured but affects only part of inflows in the tunnel section (0-100m). The second is the collecting canal flow rate, measured at the positions before and after this section, which represents the total water balance, the quantity to be compared with the model.

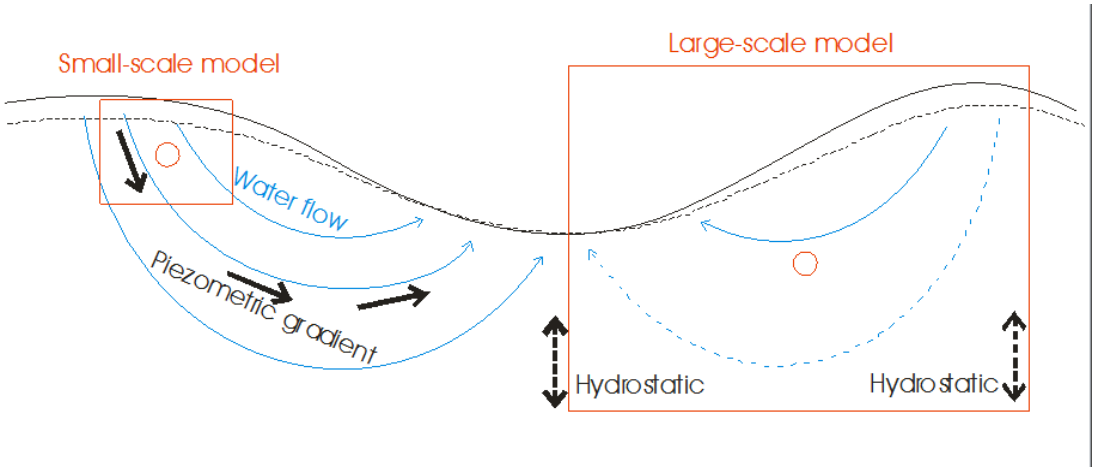

Figure 3-4: Scheme of M2-M4 models (left) and M1 (right)

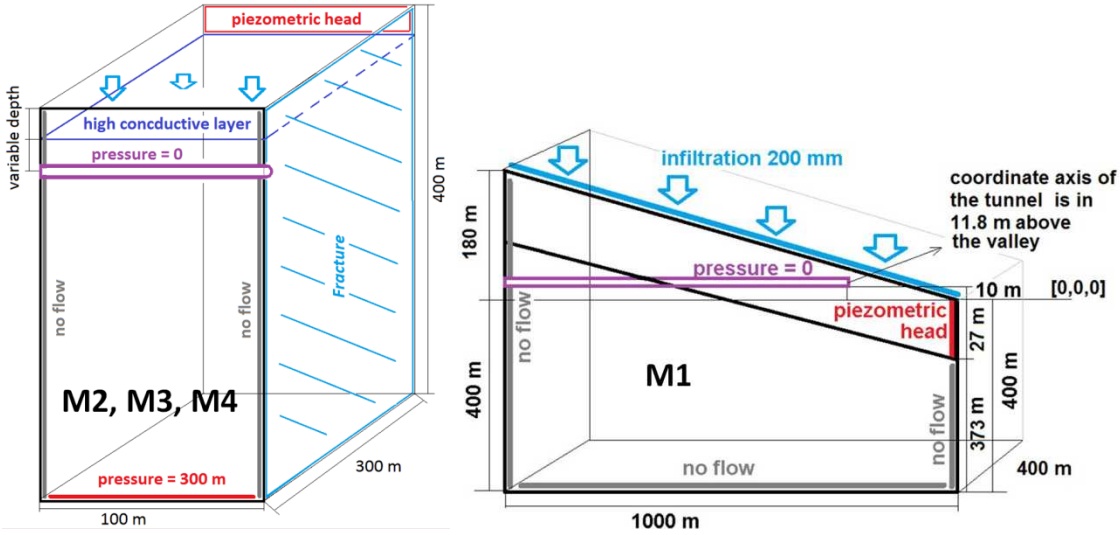

Figure 3-5: (a) The geometry and boundary condition for small-scale models M2-M3; (b) and for large-scale inclined model M1.

The case of Model 1 could not be well suited for fitting the conditions of the tunnel in the unsaturated zone, with large variations of inflow based on the surface water infiltration and expected consequent water level changes. This could be represented by simplified oblique plane topography and therefore a model combining the effects of infiltration and tunnel drainage on the water table.

3.3 SOLUTION METHOD

In this study we use PFLOTRAN, a scalable, parallel, multi-phase, multi-component, non-isothermal reactive flow and transport code to simulate multiple environmental tracer concentrations in heterogeneous 2-D and 3-D domains. For all simulations in this paper PFLOTRAN was run in the Richard's equation mode, which simulates variably saturated single phase flow and transport.

The mass balance equation for Richard's flow solved by PFLOTRAN is given by:

$$\frac{\partial}{\partial t}(\phi s q) - \bigtriangledown \cdot (\rho q) = Q_w \tag{3-1}$$

where Q_w is the total water discharge, φ is the porosity, s is the water saturation, ρ is the water density and q is the Darcy flux is given by:

$$q = -\frac{k k_r}{\mu} \bigtriangledown \cdot (p - \rho g z) \tag{3-2}$$

where k is the intrinsic permeability, k_r is the relative permeability, μ is the viscosity and g is the acceleration of gravity. The multi-component, multi-phase geochemical mass conservation equation is written:

$$\frac{\partial}{\partial t}\left(\phi \sum_{\alpha} s_\alpha \Psi_j^\alpha\right) + \bigtriangledown \cdot \sum_{\alpha} (q_\alpha - \phi s_\alpha D_\alpha \bigtriangledown) \Psi_j^\alpha = Q_i - \sum_m v_{jm} I_m - \frac{\partial S_j}{\partial t} \tag{3-3}$$

where the sum is over α fluid phases, D_α is the dispersivity tensor, Q_j is a generic source or sink term, the sum $\sum_m v_{jm} I_m$ represents the sum over all mineral reactions with stoichiometric coefficient v_{jm} and mineral reaction rate I_m and S_j is the concentration of sorbed species. Ψ_j^α is the total concentration in the α fluid phase for the primary species given by:

$$\Psi_j^\alpha = \delta_{l\alpha} C_i^l + \sum_{i=1}^{N_L} v_{ij} C_i^\alpha \tag{3-4}$$

where the l subscript denotes the liquid phase C_j^l are the primary species v_{ji} are the stoichiometeric coefficients relating the primary species to the secondary species C_i^α. The secondary species are calculated by:

$$C_i^\alpha = (\gamma_i^\alpha)^{-1} K_i^\alpha \prod_{i=1}^{N_L} (\gamma_i^l C_i^l)^{v_{ij}} \tag{3-5}$$

with equilibrium constant K_i^α and activity coefficient γ_i^α and γ_j^l.

PFLOTRAN solves Equations (1)-(5) using fully implicit, integral finite volume. PFLOTRAN is written in object oriented FORTRAN 9X and uses Message Passing Interface for distributed-memory, domain-decomposition parallelism. The Portable Extensible Toolkit for Scientific Computation (PETSc) library is leveraged to provide access to cutting edge parallel Newton-Krylov solvers. Parallel IO is achieved using the HDF5 file format. PFLOTRAN is written to be employed on a variety of architectures and scales from single processor laptops to 2^{17} core petascale simulations.

3.4 DIRECT COMPARISON STEADY STATE HYDRAULICS, TRANSIENT TRACER PULSE

M2-M4:

Model results for each team were compared used directly specified material properties for each model. The goal was to check the validity of each model. The properties for each model are specified in Table 3-2. The quadrilateral mesh for the M2 model used in the PFLOTRAN simulations is shown in Figure 3-6.

Table 3-2: Comparison Results summary

			Model 2 (V6)	Model 3 (V2)	Model 4 (V4)
	tunnel depth [m]		-39	-140	-91
	thickness of shallow zone [m]		-20	-15	-20
	K shallow [m/s]		1.00E-06	1.00E-06	1.00E-06
	K fract [m/s]		1.14E-07	1.29E-10	2.35E-08
	K deep [m/s]		5.47E-10	3.17E-12	4.04E-10
	n shallow		0.02	0.02	0.02
	n fract		0.043538	0.00004	0.073
	n deep		0.0225	0.00004	0.073
	dispersion length (L/T) (m)		5/1	5/1	5/1
	tortuosity		1	1	1
	diffusion coef. (m²/s)		6E-10	6E-10	6E-10
	TUL FVM upwind advection only presented in tab5 dec/2014		*36.6*	*147*	*300*
	TUL FVM coarse (only advection)		39.70555	147.7466	336.6703
	TUL DG coarse		45.94456	125.213	530.746
	TUL FVM fine (only advection)		43.21043		299.15
Parameter group 2	TUL DG fine		47.97367		367.00
	Sandia	MRT	45.31	138.38	210.54
POR2	BGR	[month]	47.2504	604.6081	224.5154

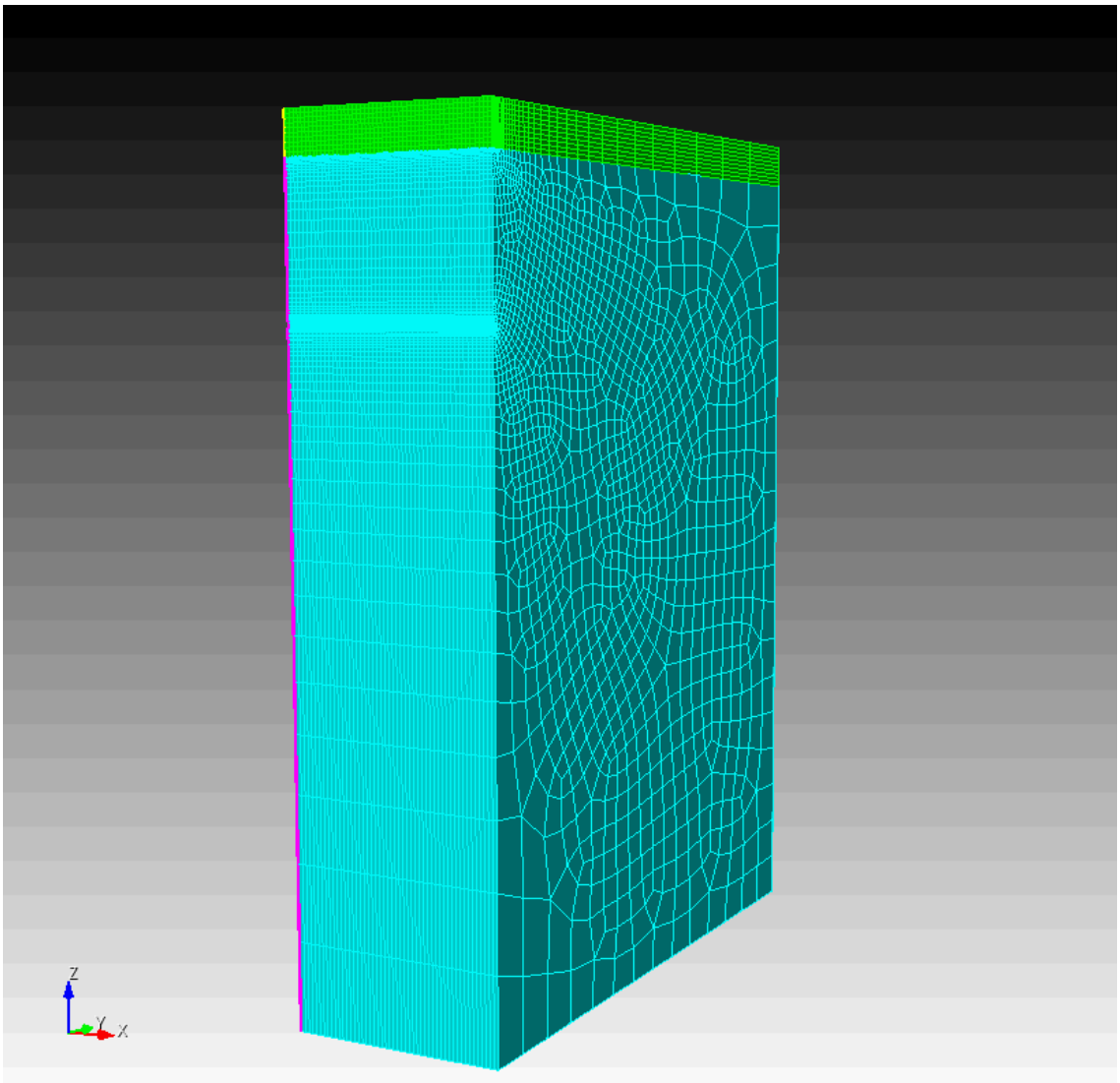

Figure 3-6: Example mesh for conceptual model 4. Total mesh elements ~ 90K, nodes ~ 96 K.

Boundary conditions for the model were assigned according to the conceptual model described above. Simulations were run for a suitable period of time to achieve steady state conditions. An example of the flow solution is shown in Figure 3-7 for the M2 simulation at steady state.

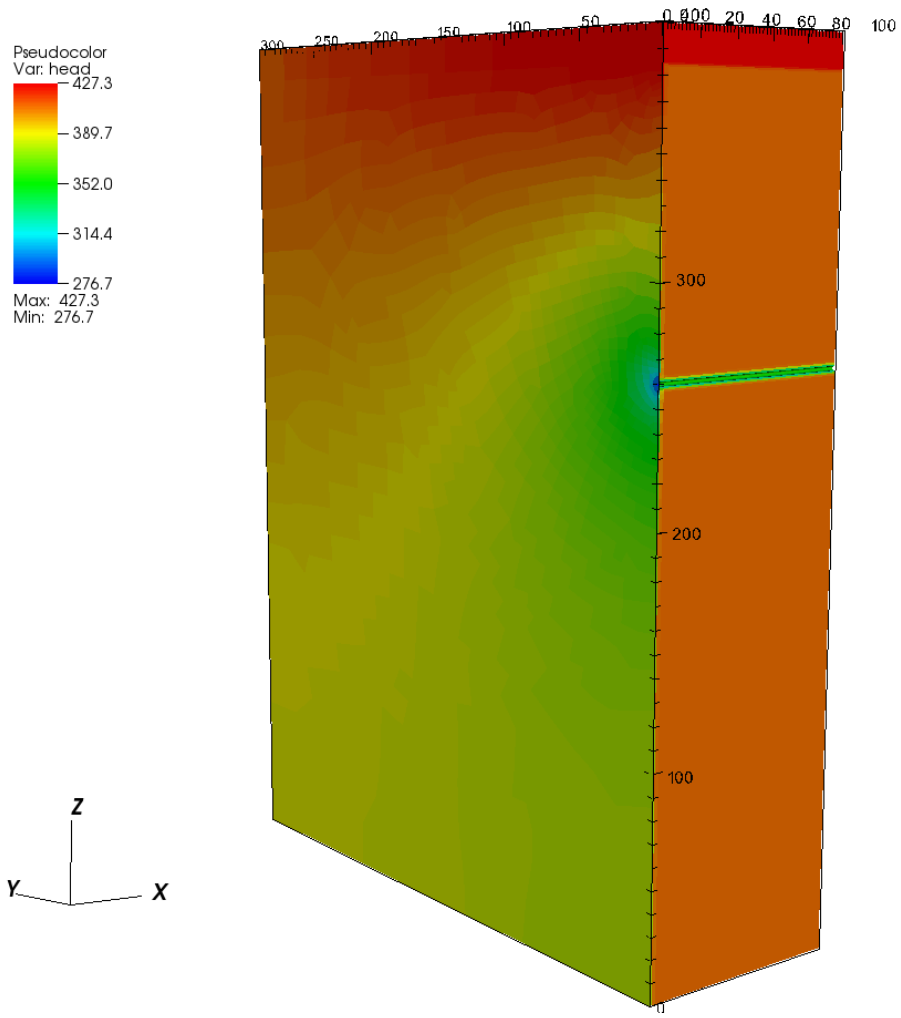

Figure 3-7: Steady state head distribution for the V2 simulation

The steady state flow field was then used in the pulse transport simulation. Here a transient dirichlet pulse of tracer is applied at the recharge boundary at time zero. The transport of the tracer pulse through the domain to the tunnel then gives the steady state travel time distribution of flow to the tunnel. An example of a time series of solute transport in the V5 simulation is given in Figure 3-8. The observed break through (travel time distribution) in the tunnel is given in Figure 3-9. The mean age is calculated as:

$$\tau_m = \int_0^\infty \frac{C(\tau)\tau}{C(\tau)} d\tau \qquad (3\text{-}6)$$

where τ is the elapsed time since the beginning of the simulation.

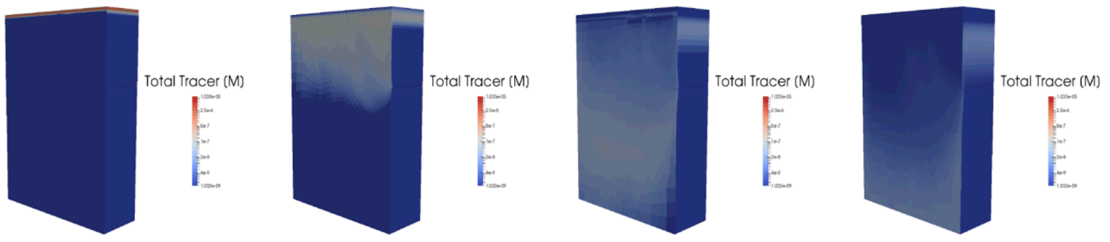

Figure 3-8: Transport sequence of tracer for the V5 simulation. Note that tracer concentration is contoured in log scale. Fracture plane on left side of domain, tunnel on right (front) of domain.

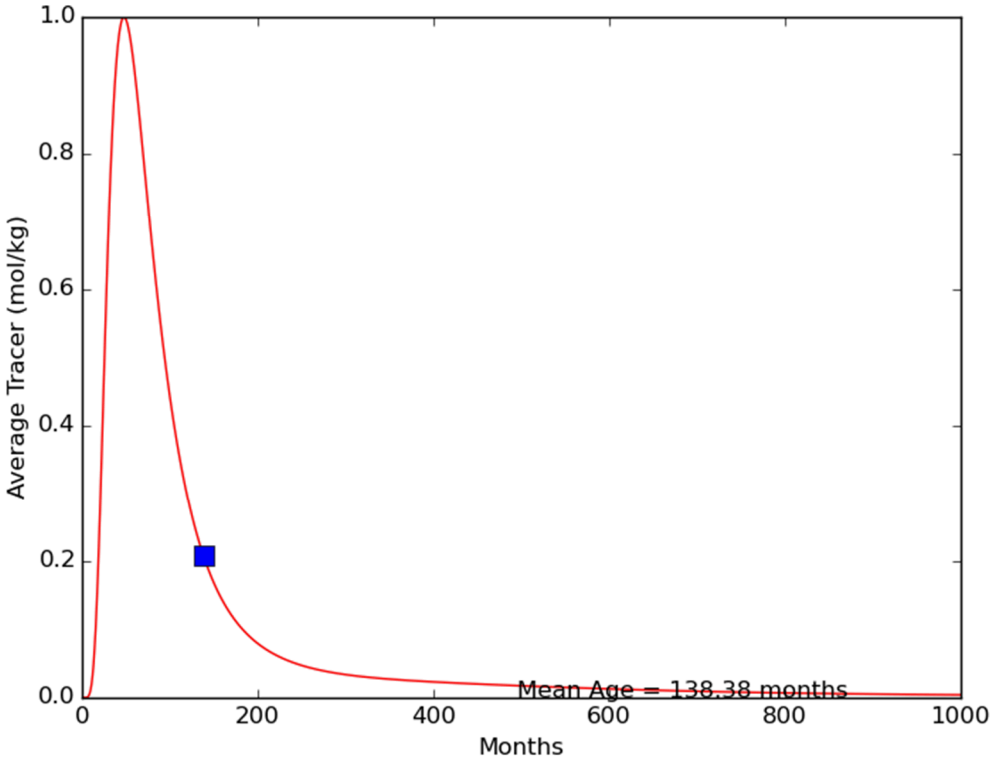

Figure 3-9: Concentration breakthrough in the tunnel and calculated mean age from the breakthrough for the V5 simulation.

The summary of the comparison results for the different teams using the prescribed model parameters is given in Table 3-2. Overall there is reasonable agreement between the teams for most simulations. The PFLTORAN results compare well with at least one team on each simulation. There is a reasonably large disagreement between teams on M3 and M4. The mechanisms for this disagreement are being discussed and evaluated. Here we use a first order calculation of the advective travel time in the fracture, to roughly estimate when the first arrival time should be expected. Here we assume the water that originates in the fracture directly above the tunnel, flows vertically from the surface to the tunnel. This approximation is reasonable given that the gradient in z at this point is order 1 while the gradient in x towards the back

aquifer is several orders of magnitude smaller. Secondly, matrix retardation should be limited in this case, because given a matrix porosity of $4x10^{-5}$, the effective diffusion coefficient is on the order of $1x10^{-14}$ m2/s, which is extremely low. Given the extremely low permeability in the matrix, velocity from the fracture to the matrix will be zero and there should be zero hydrodynamic dispersion from the fracture to the matrix. Thus, the main role of dispersion here should be to reduce the first arrival time, not to retard the mean arrival.

The first arrival time should be close to the advective travel time in fracture and can be approximated by:

$$q = K\nabla H,\ v = \frac{q}{n},\ t_{1rst} = l_{frac}/v \qquad (3\text{-}7)$$

Using K = $1.29x10^{-10}$ m/s and a unit gradient (which is the free drainage gradient to the tunnel) the velocity is around 100 m/yr in the fracture. The advective travel time for water flowing in the fracture originating directly above the tunnel is then around 15 months.

This corresponds nicely with the early arrival time in the PFLOTRAN M3 simulation, where first arrival is almost exact at 1 year, with dispersion making the earliest arrivals occur slight earlier (Figure 3-10). Using first order calculations of the first arrival time for M3, the PFLOTRAN results appear reasonable.

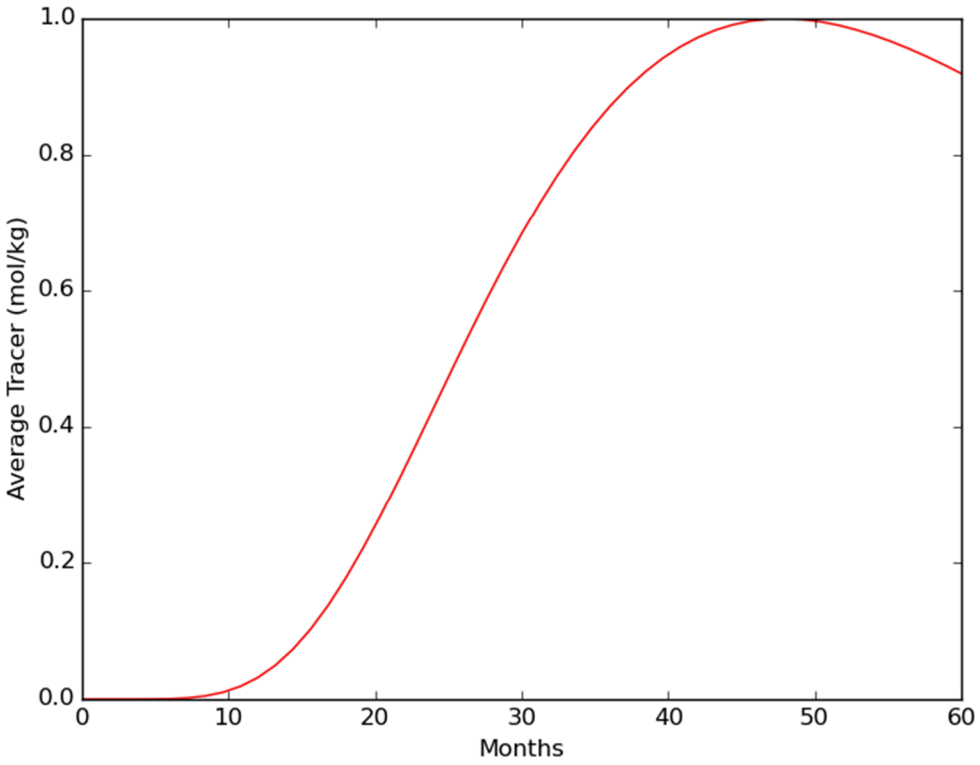

Figure 3-10: Early time breakthrough for the M3 PFLOTRAN simulation

M1

The mesh for the M1 hydrualic simulation is shown below in Figure 3-11. Boundary conditions taken from the conceptual model are also shown in Figure 3-11. Uncalibrated, preliminary parameters were used for the hydraulic simulation and are given in Table 3-3.

Table 3-3: M1 Parameters and results summary

			Model 1
	tunnel depth [m]		
	thickness of shallow zone [m]		-27
MRT	K shallow [m/s]		1.00E-06
	K deep [m/s]		1.00E-15
	n shallow		0.1
	n deep		0.01
	dispersion length (L/T) (m)		5/1
	tortuosity		0.5
	diffusion coef. (m^2/s)		1E-9
	Sandia		76.92

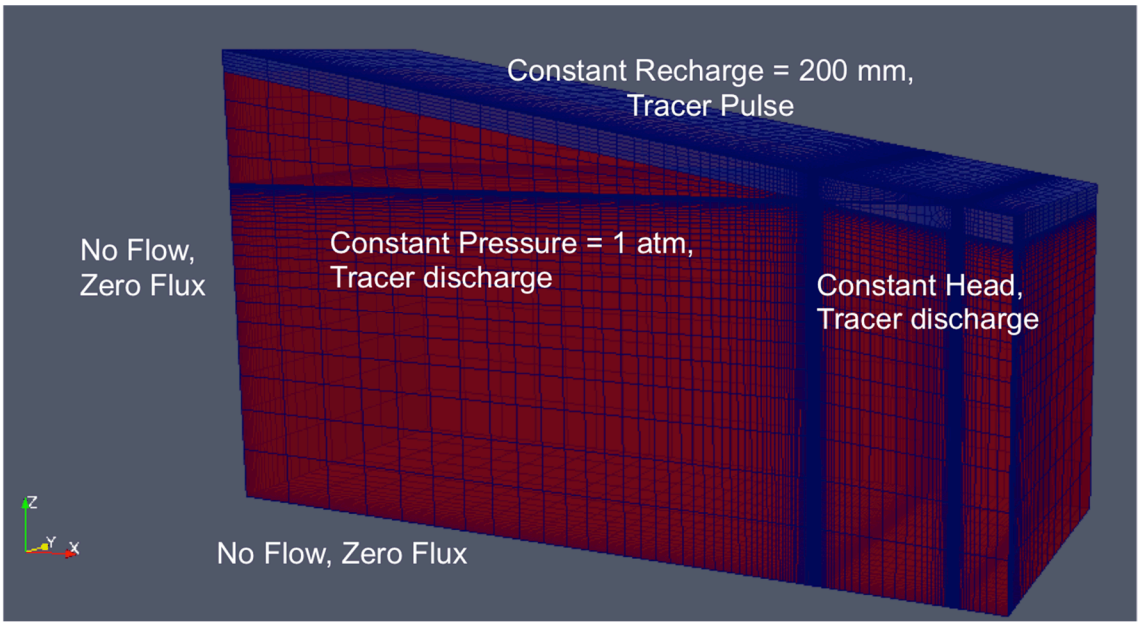

Figure 3-11: M1 mesh and boundary conditions

Hydraulic simulations were run to steady steady state. The steady state distribution of liquid saturation is given in Figure 3-12. The steady state hydraulic fluid flow field was then used for the transient pulse transport. The pulse migration is summarized in Figure 3-13.

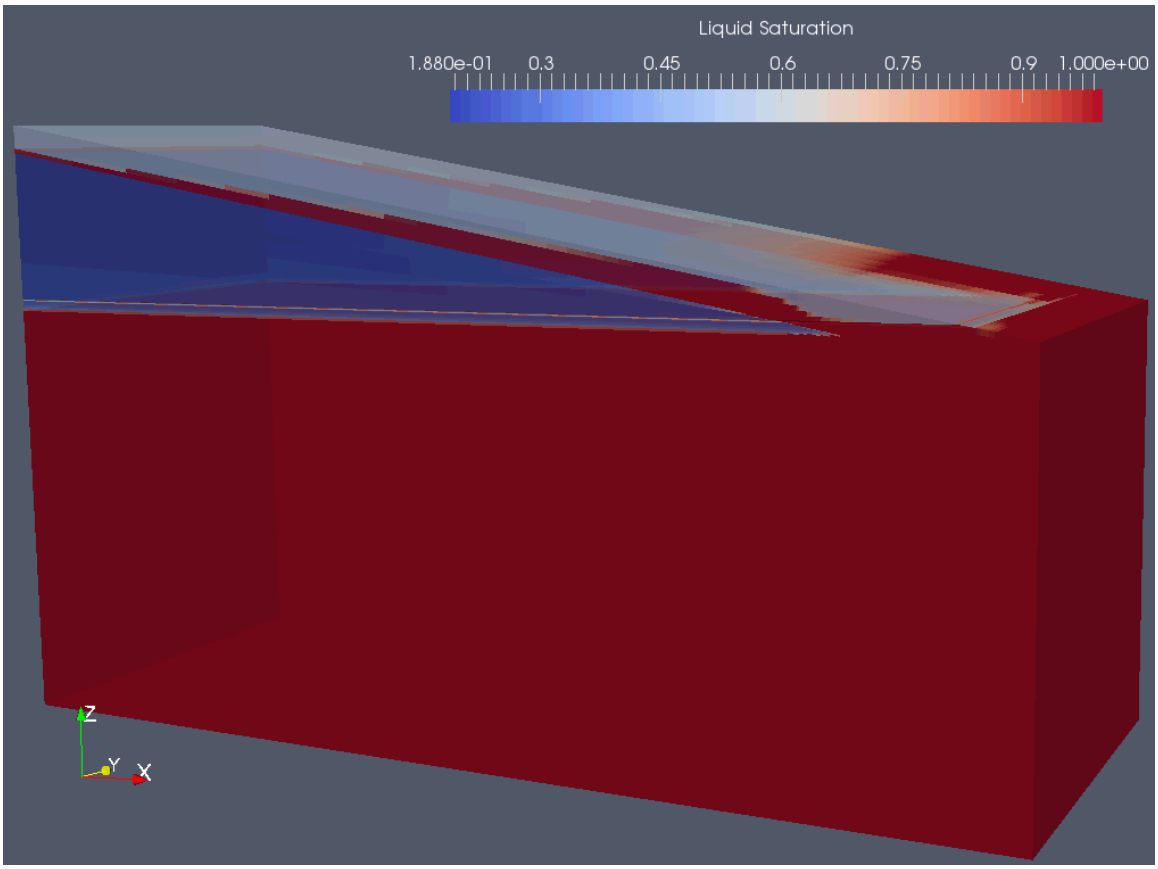

Figure 3-12: State liquid saturation for the M1 hydraulic simulation

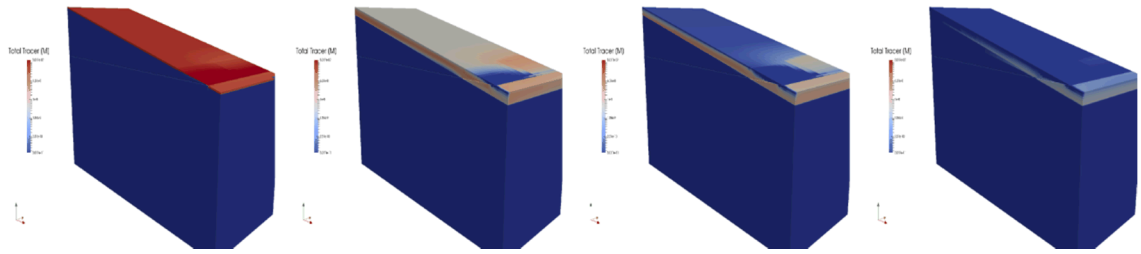

Figure 3-13: M1 pulse tracer transport sequence

The travel distribution for the M1 simulation is given in Figure 3-14, and shows a distinctly different shape than the M2-M4 models. The difference in shape is due the different flow path distributions for this model.

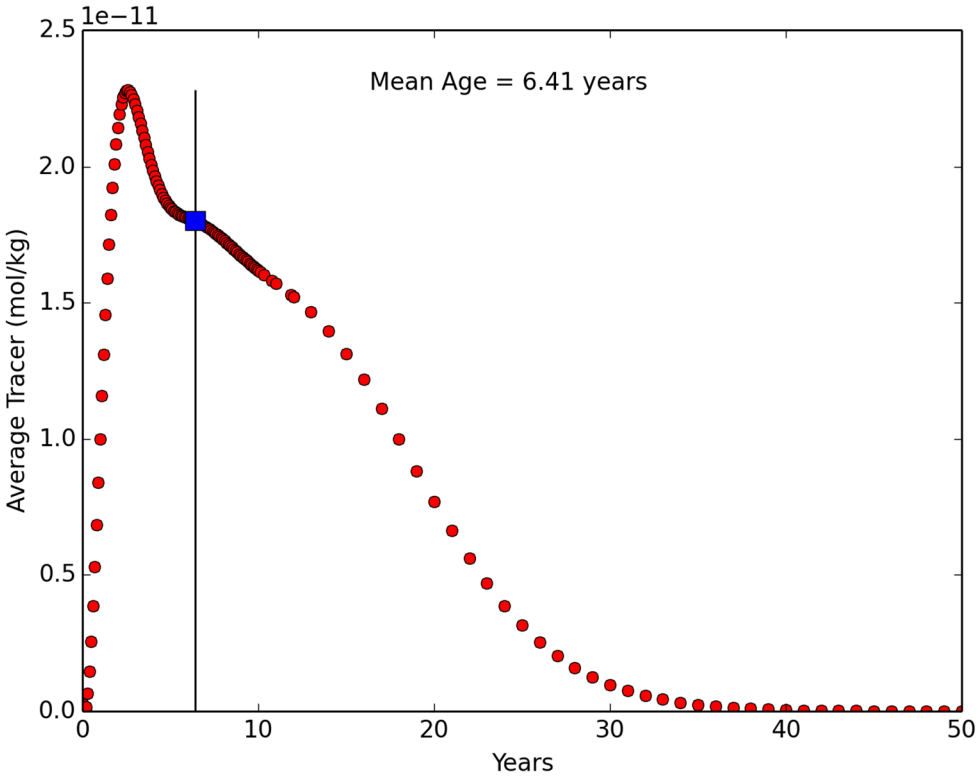

Figure 3-14: Travel time distribution for the M1 transient tracer pulse simulation

Transient Recharge, Transient Isotope Transport

In these simulations the constant recharge used in the simulations above was changed to a transient recharge set as 20% of monthly average observed precipitation at the site. The steady state hydraulic field was used as the initial condition, and then the transient recharge was applied across the top of the domain. A transient defined concentration taken as monthly average isotopic concentration was applied across the recharge zone. An annual transport sequence of $\delta^{18}O$ for M2 V6, which highlights the seasonal changes in isotopic composition and its transport through the system is shown in Figure 3-15.

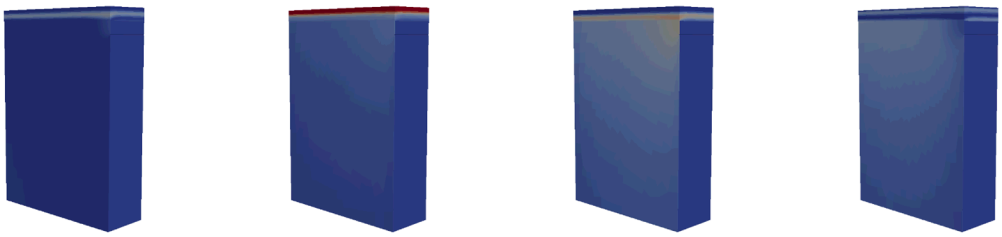

Figure 3-15: Annual transport sequence of $\delta^{18}O$ in M2 V6.

The estimated recharge, the calculated discharge and observed discharge for M2 V6 are are plotted below in Figure 3-16. Overall there is a reasonable order of magnitude match to the observed discharge, however the dynamics are not well reproduced. A probable reason is the simplified recharge function which does not accurately calculate the seasonality of recharge in the system.

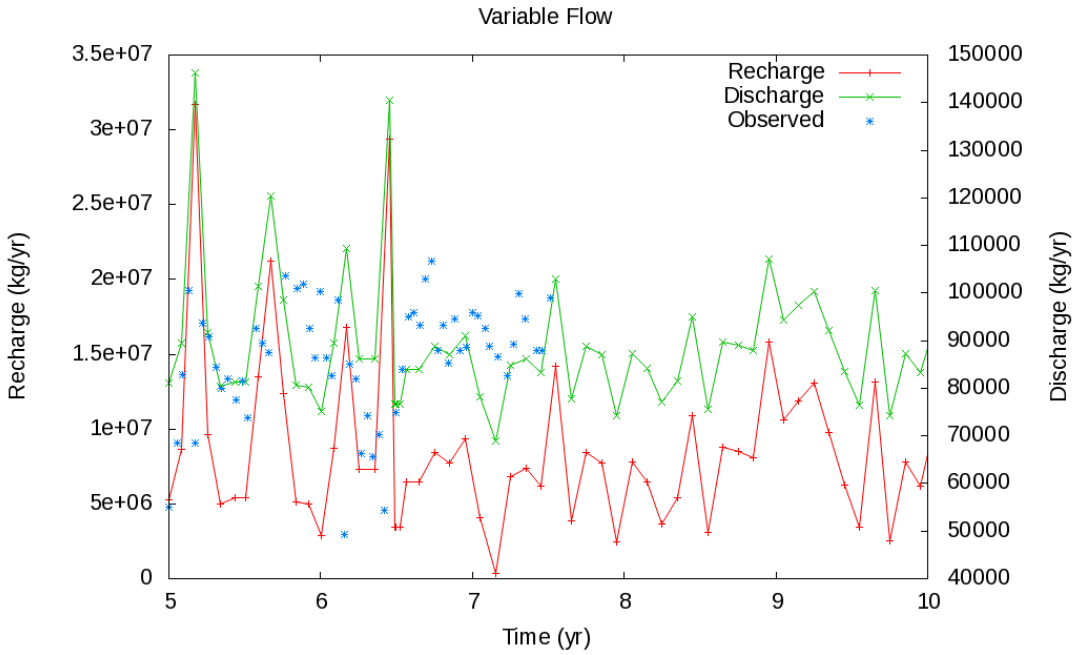

Figure 3-16: Transient recharge, modeled fracture discharge and observed discharge for M2 V6

The $\delta^{18}O$ in precipitation, the modeled outflow $\delta^{18}O$ and the observed $\delta^{18}O$ are shown in Figure 3-17. The model does a reasonable job of smoothing the input signal to match the observations; however, it does not smooth the signal quite enough. This could be due to the recharge function, or inadequate parameterization. Methods to better fit to the isotope data are being developed.

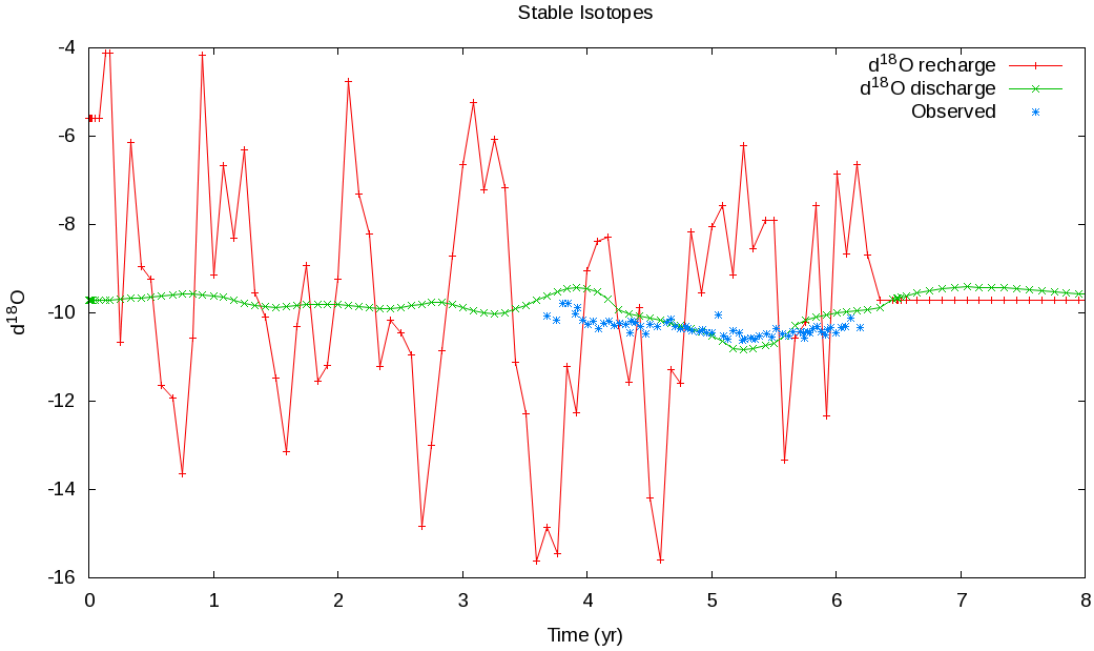

Figure 3-17: Transient $\delta^{18}O$ in precipitation, modeled $\delta^{18}O$ in the fracture outflow and the observed $\delta^{18}O$ in fracture outflow for M2 V6

The same plots of hydraulic response and isotopic composition for M3 are shown in Figures 3-18 and 3-19. Similar trends can be observed in the degree of match to the data and the inability to match certain aspects of the data.

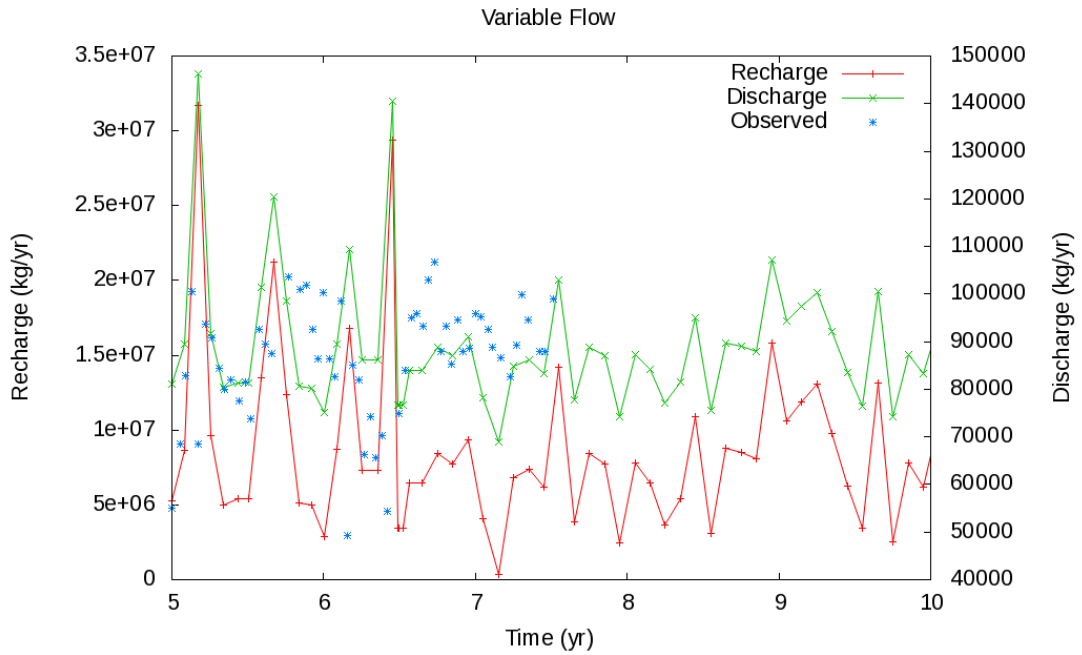

Figure 3-18: Transient recharge, modeled fracture discharge and observed discharge for M3

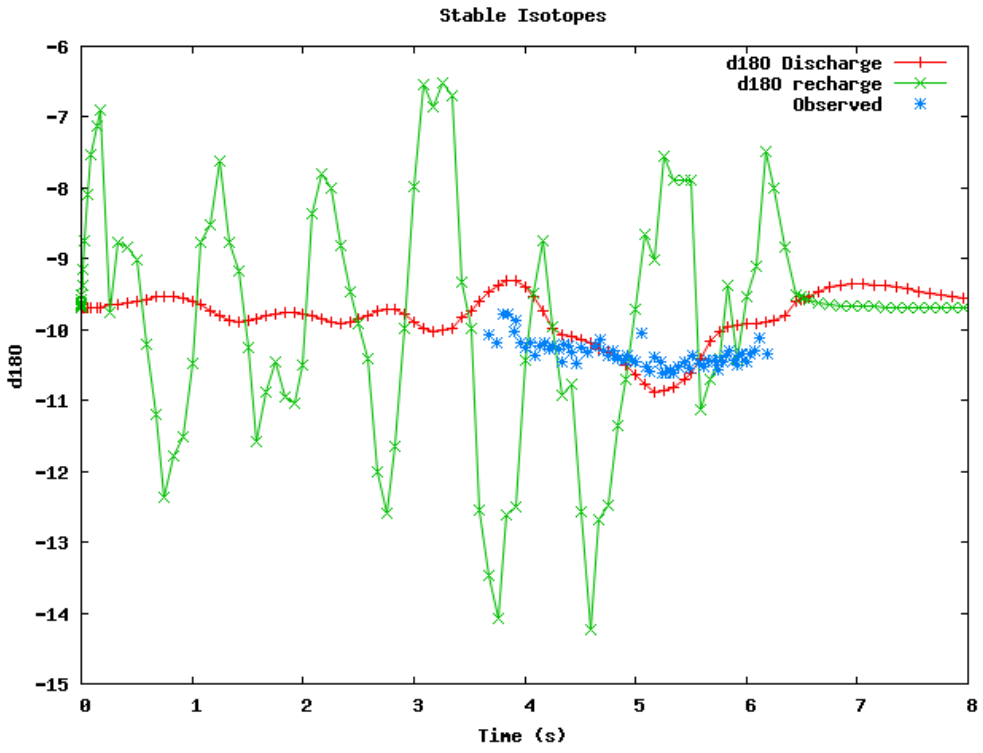

Figure 3-19: Transient $\delta^{18}O$ in precipitation, modeled $\delta^{18}O$ in the fracture outflow and the observed $\delta^{18}O$ in fracture outflow for M2 V6

3.5 CONCLUSIONS

The comparison of the models between different teams shows that for the most part the teams are able to match each other results. Understanding the discrepancies between models has proved to be a great learning experience for all teams and improved the understanding of the underlying mechanics of each code, and each codes strengths and limitations. The models reported here have been developed to understand the residence time distribution and transport properties of fractured crystalline rocks. The models are cable of reproducing the gross characteristics of hydraulic and tracer transport. The reasons for discrepancy between models and observation and methods to improve the fit are actively being explored. The DECOVALEX 2015 modeling is producing new insight into modeling transport in fracture systems over long scales and time periods of years. These types of data sets are valuable for both developing modeling techniques and understanding of long-term transport processes in fractured rock. Natural tracer data sets are of time scales much closer to repository performance prediction than most applied tracer experiments. The utilization of long-term data sets such as those provided by natural tracers allows us to gain more confidence in the prediction of long term transport.

4. FEASIBILITY OF STREAMING POTENTIAL ON ESTIMATION OF SOLUTE TRANSPORT CHARACTERISTICS OF AN AQUIFER

4.1 INTRODUCTION

Generally, fluid flow in a porous medium and then the drag of excess charge in an electrical double layer at solid-fluid interface introduce a streaming current, and the associated electrical potential is a streaming potential (SP) (Lorne et al., 1999). The SP measurement is one of the oldest methods in geophysical techniques. It consists of monitoring electrical field existing at the ground surface of the earth where the SP signals provide the evidence of polarization mechanisms existing in the grounds. The use of the SP in different aspect of geology has been developed for the last two decades and these methods have been used for a variety of geophysical applications to detect and monitor water flow (e.g., Blake and Clarke, 1999) and leakage zones of dam (e.g., Bogoslovsky and Ogilvy, 1970; Titovet al., 2000). The SP was also used to detect the ore bodies and contaminant plumes that are rich in organic matter associated with the electro redox effect (e.g., Arora et al., 2007; Jardani et al., 2008). Because the SP is directly occurred by the hydraulic gradients in porous media and is very sensitive to the actual water, however, the major contribution of SP has been to characterize fully or partially saturated media (e.g., Fournier, 1989; Mikhailov et al., 1997; Doussan et al., 2002; Suski et al., 2004; Revil et al., 2004; Jon et al., 2008).

During a hydraulic test, which is the classical method used to obtain information about the distribution of hydraulic properties of an aquifer, SP signals can be recorded at the ground surface by measuring electric potential differences between the nonpolarized electrodes by voltmeter and these electrodes are usually set up with the direction of water flow. Groundwater flows through a porous medium, and SP is changed due to excess charge of the pore water at the nearby mineral-pore water interface. The change of SP helps for detecting the fluid flow to characterize the hydraulic properties of the medium. Rizzo et al. (2004) estimated the hydraulic properties of an aquifer from hydraulic head and SP signals through numerical modeling with associated hydraulic tests. Malama et al. (2009a, 2009b) developed semi-analytical solution for transient streaming potentials associated with axial symmetric flow by pumping in the confined and unconfined aquifers.

Here we present a sandbox experiment to check the feasibility of SP to estimate solute transport characteristics of an aquifer. We conducted tracer tests under steady-state groundwater flow condition with recording SP signals. We used an acrylic tank filled with medium to coarse grained sand and infiltrated with water, and tried to detect the changes in SP signals due to injection and transport of tracer.

4.2 MATERIALS AND METHODS

Fig. 4-1 is the flow chart of this study. An acrylic tank was prepared for the experiment, and filled with homogeneous sand which was medium to coarse grained quartz sand with clay particles. Two reservoirs were connected to the sandbox, and they were upstream and downstream reservoirs which were used to control the water flow condition in the sandbox by

overflowing water from the pipe connected to the bottom of the two reservoirs. The total length of the acrylic tank was 2.5 m with the sandbox of 1.5 m, the upstream reservoir of 0.5 m and the downstream reservoir of 0.5 m, and its height was 1.0 m as shown in Fig. 4-2. The upstream and downstream reservoirs were separated from the sandbox by 200 μm stainless steel mesh. Here we used five plastic screened wells which were around 1.5 cm in diameter and 1.0 m long. These screened wells included micro holes with the diameter of 0.2 cm to infiltrate water and were covered by 200 μm plastic mesh not to fill with sand during the experiments and to collect water sample uninterruptedly (Fig. 4-2). The screened wells set parallel at the middle of the sandbox about 25 cm distances each other. The tops of the wells were open in the air, and bottoms were sealed into the sandbox. 20 sintered Ag/AgCl non-polarizing electrodes were installed at the top of the sand aquifer, and they surrounded the screened wells with definite distance of 8 cm to collect SP signals in the sandbox during the experiments (Crespy et al., 2008; Martinez-Pagan et al., 2010). Fig. 4-3 shows the setting of the instrument for the experiment.

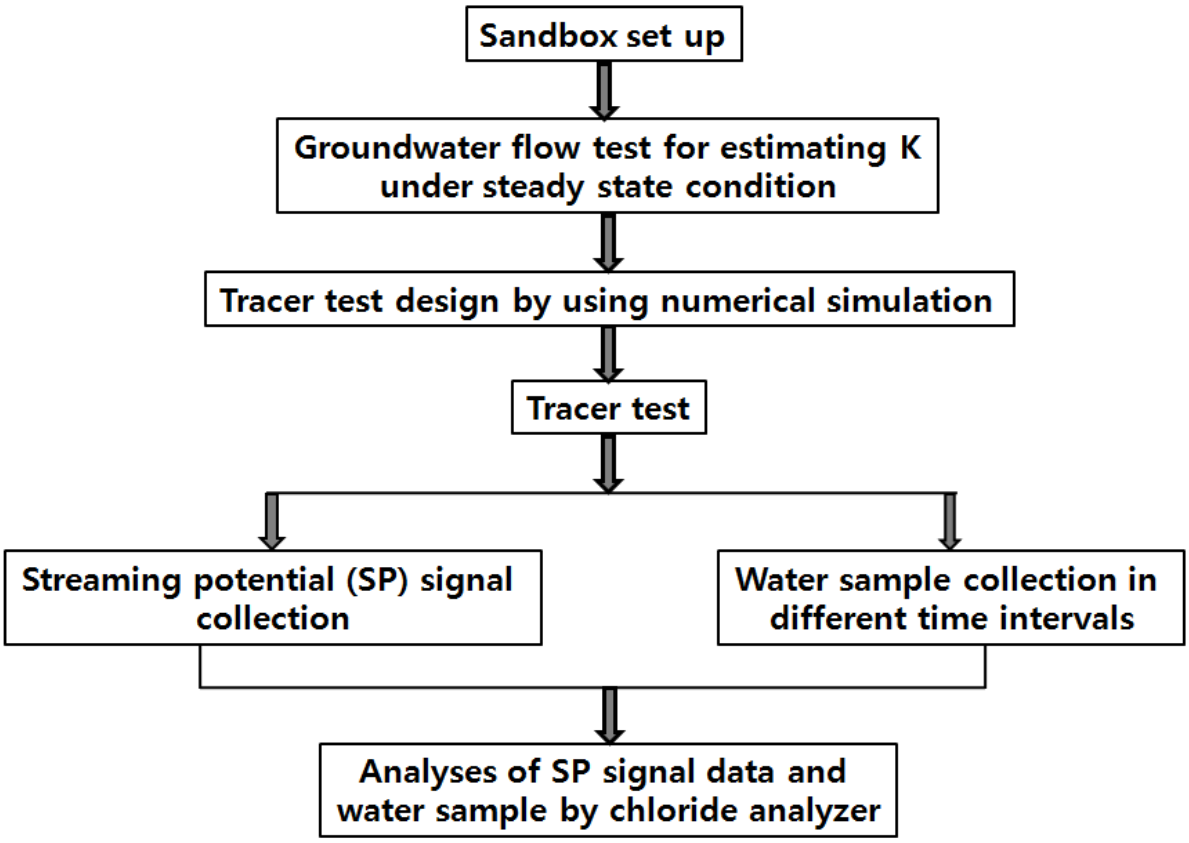

Figure 4-1: Flow chart of this study

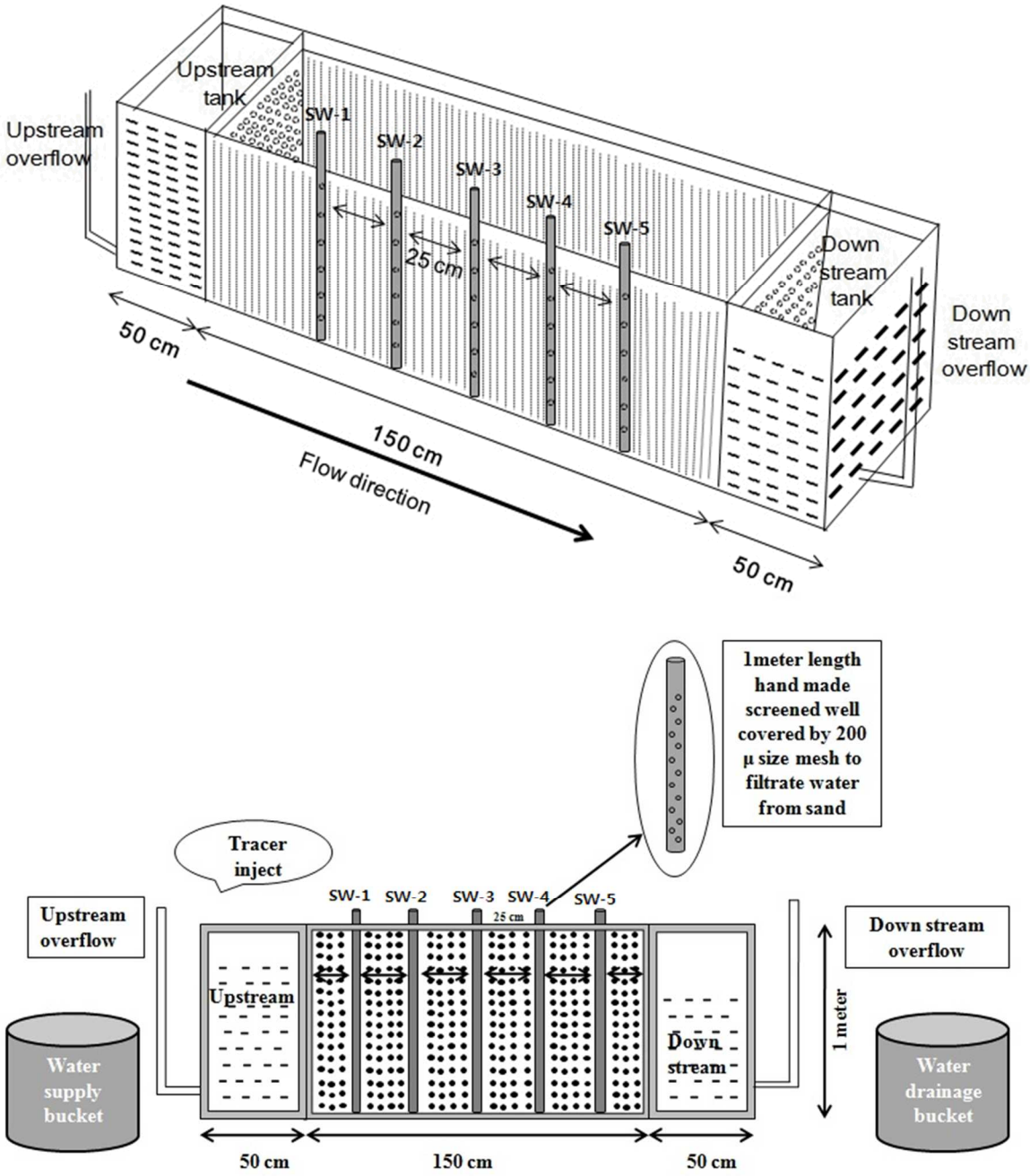

Figure 4-2. Design of the sandbox

Figure 4-3: Full set up of a sandbox experiment

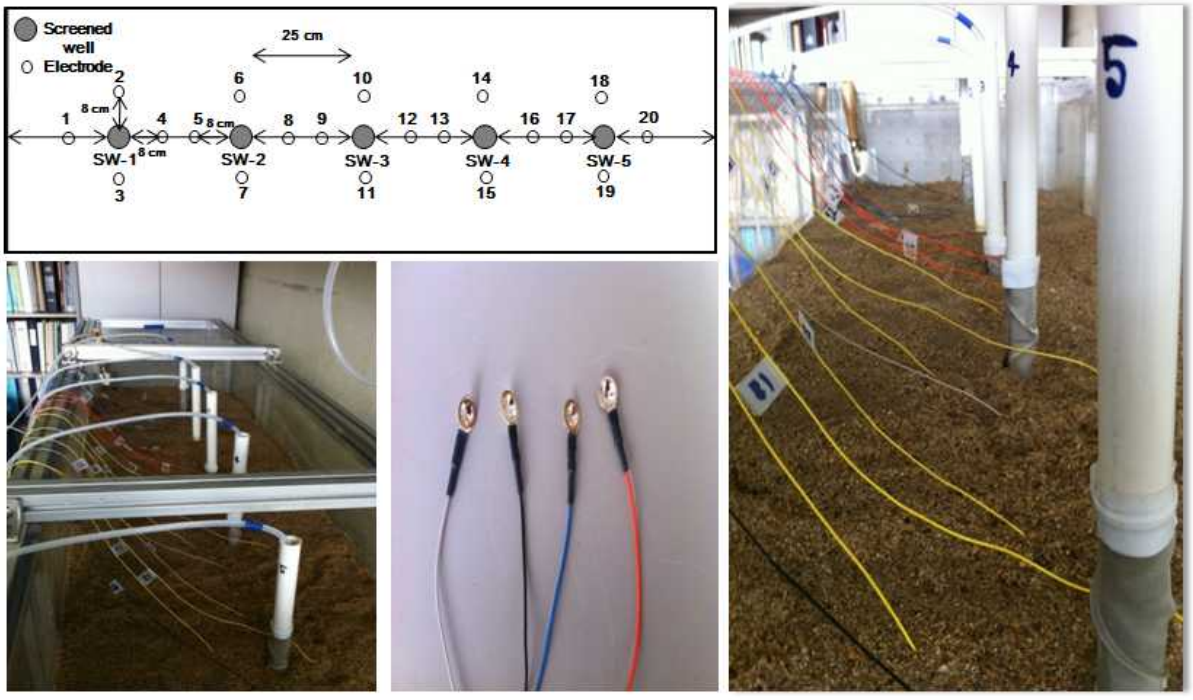

Figure 4-4: Electrode set up into the sandbox

The hydraulic conductivity of the sandbox was determined through groundwater flow tests. For the tests, the steady-state condition of groundwater flow was established by maintaining the hydraulic head difference between the upstream and downstream reservoirs. After establishing the steady-state condition, we measured the out-flow rate at the downstream of the sandbox and calculated the hydraulic conductivity using equation (4-1) which was from Darcy's law:

$$K = \frac{q}{Ai} \tag{4-1}$$

where q is the out-flow rate [m^3/sec], A is the cross sectional area of the sandbox [m^2], L is the length of the sandbox [m], H is the hydraulic head [m], and i is the hydraulic gradient given by $i = \frac{H_{upstream} - H_{downstream}}{L}$. In this study, we estimated the hydraulic conductivity with several hydraulic head differences. Using the estimated hydraulic conductivity, we simulated the tracer test for its design. From the simulation we determined the optimal injection rate and sampling intervals. In the simulation, we assumed the effective porosity and longitudinal dispersivity to 0.15 and 0.1 m, respectively, referring to Domenico and Schwartz (1990).

A tracer test was also conducted using the sandbox. NaCl solution with the concentration of 1000 ppm was used as a tracer. We injected the tracer into the second screened well for five minutes. Before and after tracer injection, water was injected to the injection well with the same injection rate to maintain the water flow condition during the whole experiment. We collected water samples from each of the five screened wells using disposable syringes, and analyzed their concentration with the chloride analyzer (Model-926, Cole-Palmer Inc.). The tracer test results were analyzed as follows. The linear velocity was calculated from the peak arrival time of the obtained breakthrough curves, and the longitudinal dispersion coefficient was introduced from the variance of the breakthrough curves using equation (4-2) (Fetter, 1992):

$$D_L = \frac{\sigma^2}{2t} \tag{4-2}$$

where D_L is the longitudinal dispersion coefficient [m^2/sec], t is the peak arrival time of the tracer [sec] and σ^2 is the variance of the breakthrough curve [m^2]. During the experiments, the change of SP signals were recorded using 20 sintered Ag/AgCl electrodes connected with a multimeter (Model-M2700, Keithly Inc.). The multimeter was connected with the computer to collect electrical signals automatically. Fig. 4-4 shows the channel numbers of each electrode installed in the sandbox. Note that we considered another electrode as a reference which was located beside the sandbox.

4.3 RESULTS AND DISCUSSION

The hydraulic conductivity of the sandbox was estimated from the groundwater flow tests with various hydraulic head differences between upstream and downstream reservoirs. From equation (4-1), the hydraulic conductivity was calculated to $2.50 \times 10^{-4} \pm 2.09 \times 10^{-5}$m/sec. Fig. 4-5 is the numerical simulation results of the tracer test for test design. The results show that the injection rate of 0.005 L/sec into the second screened well and the head difference less than 5 cm were sufficient conditions for the dimension of our sandbox. They also indicated that sampling

intervals of five minutes at first 2 hours and ten minutes for the rest of the test were enough to detect the breakthrough curves at each well.

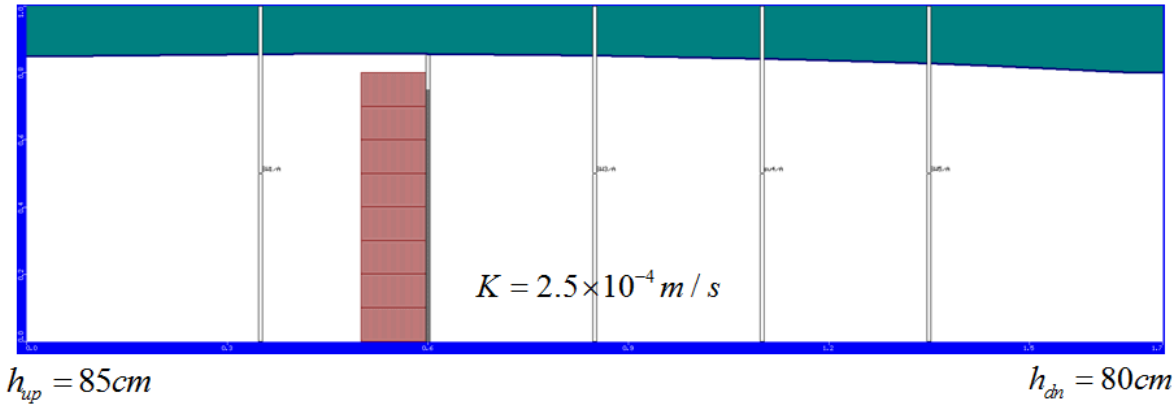

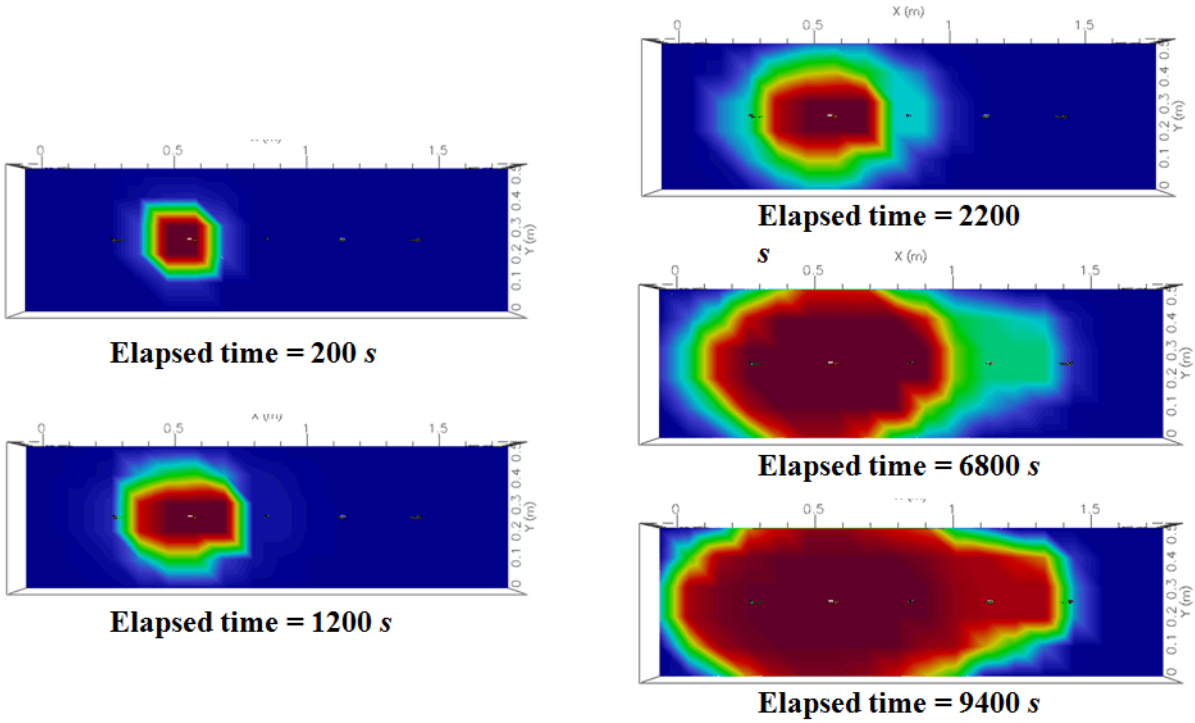

(a) Simulated water table with the injection rate of 0.005 L/sec
(b) Simulated tracer plume with the injection rate of 0.005 L/sec

Figure 4-5: Numerical simulation results of the tracer test design.

The tracer test was conducted in two phases. In the first phase, a steady-state groundwater flow condition was established by maintaining the hydraulic heads at the upstream and downstream reservoirs and by injecting water into the injection well with the designed rate. In the second phase, we injected tracer instead of water for 5 minutes, and then injected water again to maintain water flow condition. The chloride concentrations of collected water samples during the experiment were plotted in Fig. 4-6. It shows that the tracer moved slowly from the injection well to other wells. The obtained breakthrough curves were similar to the normal distribution curve although the break-through curve from the third screened well (SW-3) showed double peaks. At the fourth (SW-4) and fifth (SW-5) screened wells, it was difficult to identify the breakthrough curve. Table 4-1 shows the analysis results of the tracer test. For SW-3, the first peak of the chloride concentration was analyzed to estimate the linear velocity and dispersion coefficient. Tracer analysis results show the variation of linear velocity and dispersion coefficient in different screened wells. From the injected well to the last screened well it shows natural plume was created by the tracer solution. Here, the highest linear velocity was 5.5 $x10^{-6}$ m/sec at SW-3 and the largest dispersion coefficient was 2.8 $x10^{-4}$ m^2/sec at SW-1. However, the estimated linear velocities and dispersion coefficients were similar in the order of magnitude, respectively.

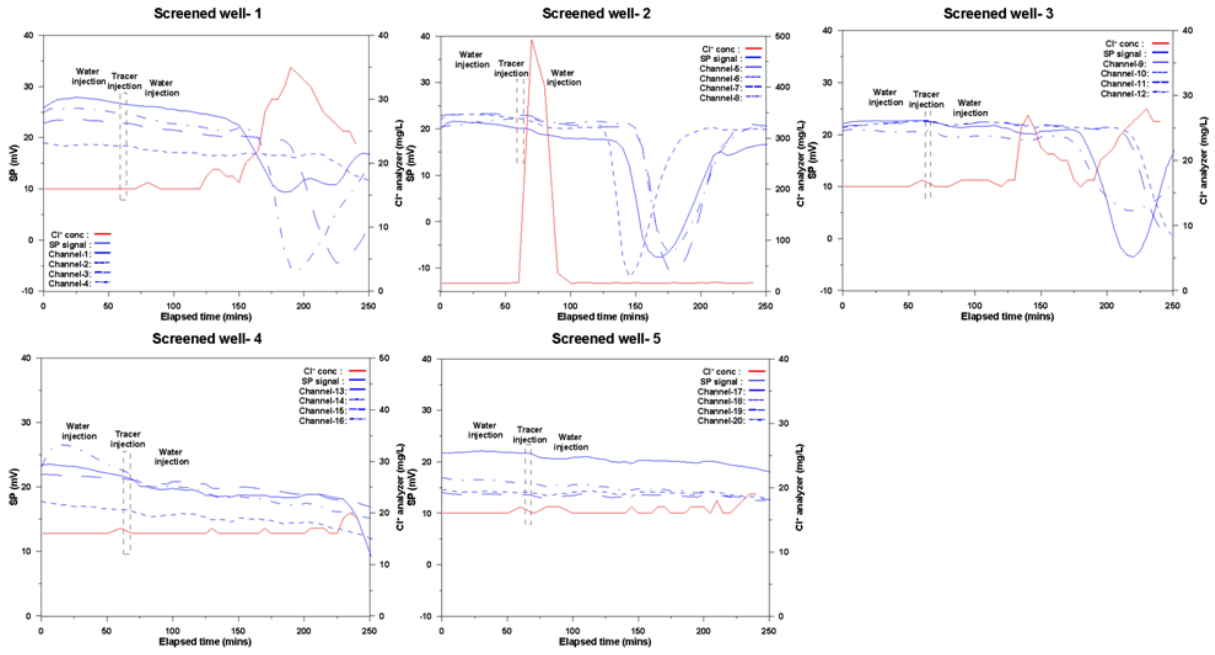

Figure 4-6: Measured SP signals and Cl^- concentrations during the experiment where black dotted boxes in the graph indicates timing of tracer injection.

Table 4-1: Analysis results of the tracer test.

Screened well	Average linear velocity, v_i (m/sec)	Hydrodynamic dispersion coefficient parallel to the direction of flow, D_L(m^2/sec)	Variance of the parallel spreading of plume, σ_L^2 (m^2)
SW-1	$3.3x10^{-6}$	$2.8 x10^{-4}$	6.46
SW-3	$5.5x10^{-6}$	$1.4 x10^{-4}$	4.07
SW-4	NA*	NA	NA
SW-5	NA	NA	NA

* Not Available

Fig. 4-6 also shows the distributions of SP signals data set measuring during the experiment. The black dotted boxes in the graphs indicate the duration of tracer injection. We did not found any significant change of SP signal dataset before the injection of tracer but we found signals responding to solute transport at SW-1, SW-2 and SW-3. At SW-1, the chloride concentration showed one peak at 180 to 200 minutes, and during that time SP signals also showed the reverse effect. Similarly, at other screened wells, the SP signals also changed when the chloride concentration changed. These results indicate that the SP signals are likely to be related to the solute transport.

4.4 CONCLUSIONS

To evaluate the feasibility of SP signals on estimation of solute transport properties of an aquifer, we conducted a tracer test with measuring SP signals. The results confirmed that the measured SP signals were produced during our experiment, and it showed significant trend or relationship between the SP and solute transport property of the sandbox during the whole period of experiment. However, we could not confirm this conclusion because there are few previous researches which provide the theoretical backgrounds of the observed phenomena in our experiments. Thus, further study to quantify the behavior of SP responding to solute transport is necessary.

Our results indicate a clue that there is a relation between SP and solute transport in an aquifer, which provides a stepping-stone for the expansion of our understanding of transport in an aquifer and reduction of the uncertainty in a tracer test.

4.5 REFERENCES

Arora, T., Revil, A., Linde, N., and Castermant, J., 2007, Non-intrusive determination of the redox potential of contaminant plumes using the self-potential method, *J. Contamin. Hydrol.*, **92**, 274– 292.

Blake, E.W. and Clarke, G.K.C., 1999, Subglacial electrical phenomena, *J. Geophys. Res.,* **104**, 7481–7495.

Bogoslovsky, V.A. and Ogilvy, A.A., 1970, Natural potential anomalies as a quantitative index of the rate of seepage from water reservoirs, *Geophys, Prospec.,* **18**, 261–268.

Crespy, A., Revil, A., Linde, N., Byrdina, S., Jardani, A., Boleve, A., and Henry, P., 2008, Detection and localization of hydromechanical disturbances in a sandbox using the self-potential method, *J. Geophy. Res.*, **113**, B01205, doi:10.1029/2007JB005042.

Domenico, P.A. and Schwartz, F.W., 1990, *Physical and Chemical Hydrogeology*, John Wiley & Sons, New York.

Doussan, C., Jouniaux, L., and Thony, J.L., 2002, Temporal variations of SP and unsaturated water flow in loam and clay soils: a seasonal field study, *J. Hydrol*., **267**, 173-185.

Fournier, C., 1989, Spontaneous potentials and resistivity surveys applied to hydrogeology in a volcanic area: Case history of the Chaine des Puys (Puy-de-Dome, France), *Geophys. Prospec.,***37**, 647–668.

Fetter, C.W., 1992, *Contaminant Hydrogeology*, Department of Geology, University of Wisconsin-Oshkosh.

Jardani, A., Revil, A., and Dupont, J.P., 2008, Three-dimensional inversion of self-potential data used to constrain the pattern of groundwaterflow in geothermal fields, *J. Geophys. Res.,* **113**, 1-22.

Jon, H., Saunders, L., Matthew, D., Jackson, L., and Christopher, C.P., 2008, Fluid flow monitoring in oil fields using downhole measurements of electrokinetic potential, *Geophysics*, **73**, 165-180.

Jouniaux, L., Maineult, A., Naudet. V., Pessel, M., and Sailha, P., 2009, Review of self-potential methods in hydrogeophysics, *Critical Review Geosciences*, **341**, 928-936.

Lorne, B., Perrier, F., and Avouac, J.P., 1999, Streaming potential measurements 1. Properties of the electrical double layer from crushed rock samples, *J. Geoph. Res.,* **104**, 17,857–17,877.

Maritinez-Pagan, P., Jardani, A., Revil, A., and Haas, A., 2010, Self-potential monitoring of a salt plume, *Geophysics*, **75**, WA17-WA25.

Mikhailov, O.V., Queen, J.H., and Toksoz, M.N., 1997, Using borehole electro seismic measurements to detectandcharacterize fractured (permeable)zones, *Annual Technical Report*.

Malama, B., Revil, A., and Kristopher, L.K., 2009a, Asemi-analytical solution for transient streaming potentials associated with confined aquifer pumping tests, *Geophys. J. Int*., **176**, 1007-1016.

Malama, B., Kristopher, L.K., and Revil, A., 2009b, Theory of transient streaming potentials associated with axial-symmetric flow in unconfined aquifers, *Geophys. J. Int*., **179**, 990-1003.

Revil, A., Naudet, V., and Meunier, J.D., 2004, The hydroelectric problem of porous rocks: Inversion of the position of the water table from self-potential data, *Geophys. J. Int*., **159**, 435–444.

Rizzo, E., Suski, B., Revil, A., Straface, S., and Troisi, S., 2004, Self-potential signals associated with pumping-tests experiments, *J. Geoph. Res.*, **109**, B10203.

Suski, B., Rizzo, E., and Revil, A., 2004, A sandbox experiment of self-potential signals associated with pumping test, *Vadose Zone J.*, **3**, 1193-1199.

Titov, K., Loukhmanov, V., and Potapov, A., 2000, Monitoring of water seepage from a reservoir using resistivity and self-polarization methods: Case history of the Petergoph fountain water supply system, *First Break*, **18**, 431–435.

5. SUMMARY

The international collaboration on the evaluation of crystalline disposal media at SNL in FY15 was focused on the following three activities: (1) thermal-hydrologic-mechanical-chemical modeling single fracture evolution; (2) simulations of flow and transport in Bedrichov Tunnel, Czech Republic, and (3) streaming potential testing at KAERI Underground Research Tunnel. The first two activities are part of the DECOVALEX project. The major accomplishments include:

- *DECOVALEX C.1: Thermal-Hydrologic-Mechanical-Chemical (THMC) Processes in Single Fractures:* A mechanistic understanding of fracture opening and closure in geologic media is of significant importance to subsurface resource extraction and waste isolation (e.g. radioactive waste disposal and carbon sequestration and storage). It has been observed that, under certain circumstances, a fracture can undergo either opening or closure or switch from one regime to another. Fracture evolution involves a complex set of coupled physical and chemical processes, including stress-mediated mineral dissolution and precipitation, fluid flow and transport, mechanical deformation, etc. A dynamic model for subsurface fracture opening and closure was formulated. The model explicitly accounts for the stress concentration around individual aperture channels and the stress-activated mineral dissolution and precipitation. A preliminary model analysis has demonstrated the importance of the stress-activated dissolution mechanism in the evolution of fracture aperture in a stressed geologic medium. The model provides a reasonable explanation for some key features of fracture opening and closure observed in laboratory experiments, including a spontaneous switch from a net permeability reduction to a net permeability increase with no changes in experimental conditions.
- *DECOVALEX C.2: Bedrichov Tunnel Test Case:* A lumped parameter model was developed for stable isotope, tritium and CFC-12 transport at the site and modeled results were compared to measured data. Code PFLOTRAN was used to simulate multiple environmental tracer concentrations in heterogeneous 2D and 3D domains. The comparison of the models between different teams shows that for the most part the teams are able to match the results among each other. Understanding the discrepancies between models has proved to be a great learning experience for all teams and improved the understanding of the underlying mechanics of each code, and each codes strengths and limitations. The models reported here have been developed to understand the residence time distribution and transport properties of fractured crystalline rocks. The models are capable of reproducing the gross characteristics of hydraulic and tracer transport. The reasons for discrepancy between models and observation and methods to improve the fit are actively being explored. The DECOVALEX 2015 modeling is producing new insight into modeling transport in fracture systems over long scales and time periods of years. These types of data sets are valuable for both developing modeling techniques and understanding of long-term transport processes in fractured rock. Natural tracer data sets are of time scales much closer to repository performance prediction than most applied tracer experiments. The utilization of long-term data sets such as those provided by natural tracers allows us to gain more confidence in the prediction of long term transport.

- *KAERI Underground Research Tunnel Tests:* SNL and KAERI have developed a multi-year plan for joint field testing and modeling to support the study of high-level nuclear waste disposal in crystalline geologic media. The work for FY15 is focused on two tasks: (1) streaming potential (SP) testing, and (2) technique development for in-situ borehole characterization. A sandbox experiment was established at KAERI to study the hydroelectric coupling in case of a tracer test. An acrylic tank was filled up with homogeneous sand as a sand aquifer, and the upstream and downstream reservoirs were connected to the sand aquifer to control the hydraulic gradient. Under a steady-state water flow condition, a tracer test was performed in the sandbox with the help of peristaltic pump, and tracer samples were collected from the same interval of five screened wells in the sandbox. During the tracer test, SP signals resulting from the distribution of 20 nonpolarizable electrodes were measured at the top of the tank by a multichannel meter. The results showed that there were changes in the observed SP after injection of tracer, which indicated that the SP was likely to be related to the solute transport. For Task 2, SNL have finalized a new contract with KAERI on a collaborative work the development of in-situ hydrological and geochemical measurements in boreholes. This task is a jointed effort between the UFD deep borehole disposal work package and the crystalline disposal R&D work package.
- *Joint Fuel Cycle Studies (JFCS):* A technical exchange meeting was held under the JFCS bilateral between the Republic of Korea (ROK) and the US DOE. Extensive technical data exchanges between the two parties have proceeded.